Acta Materialia 244 (2023) 118561

Contents lists available at ScienceDirect

Acta Materialia

journal homepage: www.elsevier.com/locate/actamat

Full length article

Insights into the stress corrosion cracking resistance of a selective laser melted 304L stainless steel in high-temperature hydrogenated water

Shihao Zhang [a], Shengkai Wang [a], Xingyu Feng [a], Zehao Ning [a], Juan Hou [b], Wenjun Kuang [a,*]

[a] Center for Advancing Materials Performance from the Nanoscale (CAMP-Nano), State Key Laboratory for Mechanical Behavior of Materials, Xi'an Jiaotong University, Xi'an 710049, China

[b] School of Materials Science and Chemistry, University of Shanghai for Science and Technology, Shanghai 200093, China

ARTICLE INFO

Keywords:
Selective laser melting
Austenitic stainless steel
High-temperature water
Dislocation cell
Stress-corrosion cracking

ABSTRACT

Selective laser melting (SLM) offers unprecedented advantages in manufacturing complex components used in nuclear reactors, and thus has promising application in the nuclear power industry. The compatibility of printed materials with typical reactor coolant should be carefully investigated as the printed materials possess unique microstructure features (e.g. columnar grain, dislocation cell and inclusion) which would inevitably affect the performance. In this work, the stress corrosion cracking (SCC) susceptibility of selective laser melted (SLMed) 304L stainless steel (SS) was evaluated in high-temperature hydrogenated water through slow strain rate tensile test and compared with two wrought 304 SSs. Interestingly, the SLMed 304L SS showed much lower SCC susceptibility than the two wrought 304 SSs, and this finding was mainly ascribed to its optimized composition. From the aspect of corrosion, the intergranular oxidation resistance of SLMed 304L SS is significantly improved due to the reduced contents of Si and Mn. In addition, the high dislocation density in SLMed 304L SS can accelerate the diffusion of solute atoms, thus further enhancing the resistance to intergranular oxidation and promoting the precipitation of oxide inside the crack which barricades the ingress of corrosive media. As for the mechanical aspect, under the combined effects of dislocation cells and nano-oxide inclusions, the SCC initiation can be alleviated as the dislocation motion in the grain matrix is hindered and planar slip is suppressed. Therefore, the optimized chemical composition and printed microstructure render this SLMed 304L SS more resistant to SCC initiation.

1. Introduction

Selective laser melting (SLM), as a promising advanced manufacturing technique, has been widely explored in a number of important fields (such as medical, aerospace and energy) in the past decade [1,2]. Like other additive manufacturing (AM) or 3D printing techniques, SLM is guided by the digital computer-aided design (CAD) through layer-by-layer strategy from bottom to top, which imparts great flexibility and freedom during manufacturing [3–5]. More importantly, AM technique such as SLM can be used to fabricate near-net-shaped and complex components that can't be made through traditional manufacture methods. SLM is highly desirable for producing complex components used in nuclear power plant because it can greatly reduce the period of time from design to production [6]. Such manufacturing process can be conveniently implemented during the reactor maintenance or refueling outages, which can avoid unnecessary delay in component replacement and improve the economy of reactor. However, the material produced by SLM possesses drastically different microstructure and mesostructure than its traditional wrought counterpart [7–9]. The performance of material would be inevitably affected and should be carefully evaluated in the relevant service environment.

Austenitic stainless steel (SS) such as 304/304L SS is the main structure material for pressure boundary as well as many core internal components in light water reactors (LWRs) due to its good machinability and high corrosion resistance in high temperature water [10,11]. The production of complex SS components in LWR is a good application scenario for SLM and has received intensive research attention recently [12–15]. It should be noted that non-equilibrium structure features such as molten pool, columnar crystal, porosity, inclusions and dislocation cells are normally generated during the SLM process [16]. Such structure features can significantly impact the performance of printed material. Up to now, massive research was focused on the evolution of

* Corresponding author.
E-mail address: wjkuang66@gmail.com (W. Kuang).

https://doi.org/10.1016/j.actamat.2022.118561
Received 27 July 2022; Received in revised form 23 November 2022; Accepted 26 November 2022
Available online 27 November 2022
1359-6454/

microstructure, mechanical behavior and room temperature corrosion behavior of printed SS [17–20], while the study of corrosion behavior in the LWR relevant service environment, i.e. high temperature water, is very limited. For printed SS intended for nuclear application, special attention should be paid to stress corrosion cracking (SCC) which is a major environmental degradation mode for this type of material in LWR environment from the past experience [10,21,22]. Lou et al. [12,14] evaluated the SCC propagation behavior of SLMed 316L SS in boiling water reactor (BWR) environment and found that the crack growth rate (CGR) is the highest when the crack propagation path is parallel to the building direction (BD). They also reported that SCC susceptibility could be increased by the preferential dissolution of oxide inclusions along the grain boundaries (GBs). Song et al. [15] investigated the effect of proton irradiation on the SCC behavior of SLMed 316L SS using slow strain rate tensile (SSRT) test in BWR environment and reported that printed SS has a lower susceptibility to irradiation-assisted SCC (IASCC) compared with wrought SS. Recent work by McMurtrey et al. [23] shows that 316L SS made by direct energy deposition (DED) has lower IASCC susceptibility than the wrought counterpart in BWR environment as the inclusions (referred as 'voids') in DED SS can suppress the irradiation damage and inhibit the localized deformation. These research results indicate that printed SS is a promising structure material in LWR environment.

Previous research on the performance of printed SS is still very limited, especially the SCC behavior which was mainly investigated in BWR environment. There is still very little work on the SCC of printed SS in pressurized water reactor (PWR) environment at present. The correlation between the performance of printed SS in typical service environment and the unique micro/mesostructure features generated by printing should be established. Such information is vital for optimizing or codifying the process parameter of printing which dictates the structure of printed material. More extensive research work needs to be done in this regards. In this paper, we evaluated the SCC initiation susceptibility of a SLMed 304L SS in simulated PWR primary water through SSRT test and compared it with the performances of two traditional wrought nuclear-grade 304 SS. Then the SCC initiation behavior of SS is discussed in relation to the chemical and microstructure features.

2. Experimental

2.1. Materials and heat treatments

In this study, gas-atomized 304L stainless steel powder with particle size ranging from 10 to 53 μm, was used to print 304 L SS blocks by SLM. The SLM process was carried out on an EOS M290 machine, with a laser power of 220 W, a scan speed of 1.2 m/s, and a layer thickness of 40 μm. The blocks were printed in an ultra-high purity Ar atmosphere where the oxygen content was less than 2000 ppm. Some of the SLMed 304L SS block was annealed at 1200 °C for 30 min and finally water quenched (SLMed 304L-1200) to alter the as-printed microstructure. The measured chemical composition of the SLMed 304L SS is given in Table 1, together with the two solution-annealed nuclear grade wrought SSs (304-A and 304-B).

2.2. Sample preparation

SLMed 304L SS, SLMed 304L-1200 SS, 304-A SS and 304-B SS were cut into dog-bone-shaped flat tensile specimens by electric-discharge machining. The tensile direction of SLM 304L SS specimen was perpendicular to the BD (for SCC initiation test, the cracking susceptibility of sample is higher when strained along this direction as more GBs are normal to the tensile direction [15]). The tensile specimens have a gage length of 15 mm, a rectangular gage cross section of 2.2 mm × 1.6 mm. Coupons were also extracted from the bulk materials with the same sampling direction as the tensile specimen. The tensile samples and coupons were mechanically ground with SiC papers down to 2000 grit, and then electropolished to remove the deformed layer. Electropolishing was performed at 35 V in methanol solution with 10 vol% perchloric acid at room temperature. All the samples were checked using SEM to ensure that no intergranular attacks were induced by electropolishing. Transmission electron microscopy (TEM) disks were prepared using a MTP-1A magnetic-driven type twin-jet electro polisher in methanol solution with 10 vol% perchloric acid at −30 °C and 30 V.

2.3. Slow strain rate tensile test and corrosion test

For evaluating the resistance to SCC initiation of these SSs, SSRT test was conducted in 320 °C, 15 MPa high purity water containing 2.7 ppm hydrogen in a refreshed SS autoclave. Once the parameters were stable, tensile specimens were strained at an initial strain rate of $2.8 \times 10^{-4} s^{-1}$ until the stress approached 80% of the yield strength of the samples. Then the strain rate was decreased to $5 \times 10^{-8} s^{-1}$. Fiducial marks were made on each tensile sample prior to SSRT test which were used to measure the real applied plastic strain after the test. Each sample was pulled to a normal plastic strain of 5.5% (corresponding to approximately a real plastic strain of 5.0%) from the real-time stress-strain curve generated from the data acquisition computer. The measured real plastic strains and test durations for each sample were listed in Table 2. The relative difference in the real plastic strain between these samples is under 5%. The un-stressed coupons were exposed in the same water environment for 622 h.

Table 2
SSRT test conditions and plan-view crack measurement results in 320 °C high purity water containing 2.7 ppm hydrogen.

SCC parameters	Samples			
	SLMed 304L	SLMed 304L-1200	304-A	304-B
Plastic deformation (%)	5.04	4.82	~5.0	4.98
Stress at target strain value (MPa)	415	231	305	274
Corrosion duration (h)	572	519	424	433
Average crack length (μm)	5.1 ± 0.2	13.8 ± 0.4	22.7 ± 0.7	10.7 ± 0.1
Crack density (mm^{-2})	5038.3 ± 548.2	1012.0 ± 53.9	516.1 ± 28.4	1626.2 ± 39.4
Crack length per unit area ($\mu m \cdot mm^{-2}$)	25852.8 ± 812.8	14062.6 ± 749.1	11761.4 ± 647.9	17536.7 ± 424.5
Average grain size (μm)	14.3 ± 4.2	51.8 ± 9.4	46.8 ± 14.3	44.6 ± 10.9
Grain boundary length density ($\mu m \cdot mm^{-2}$)	226240.0	46670.0	60284.4	61902.4
Percentage of grain boundary cracking (%)	11.43 ± 0.78	30.13 ± 0.56	19.51 ± 0.54	28.33 ± 0.28

Table 1
Chemical compositions (wt.%) of SLM 304L SS, 304-A SS and 304-B SS.

Material	C	N	Si	Mn	P	S	Cr	Ni	Mo	O	Fe
SLMed 304L	0.014	0.013	0.065	0.054	0.027	0.003	19.07	9.62	0.83	0.031	Bal
304-A	0.032		0.570	1.680	0.027	0.005	20.76	9.53	0.22		Bal
304-B	0.029		0.380	1.720	0.023	0.005	18.89	9.65			Bal

2.4. Microstructure characterization

General microstructural characterization of the specimens was performed using a FEI Verios 460 and a Hitachi SU6600 SEMs in back-scattered electron (BSE) and secondary electron (SE) modes. Electron back-scattered diffraction (EBSD) analysis of original microstructure was performed in a FEI Helios NanoLab 600 focus ion beam (FIB)-SEM system equipped with an Oxford Nordlays EBSD detector. The beam voltage, probe current and scanning step size were set to 30 kV, 5.5 nA and 0.5 μm (for SLMed 304LSS and SLMed 304L-1200 SS) or 1.5 μm (for 304-A SS and 304-B SS), respectively. Detailed microstructural characterization of dislocation cells was imaged in a JEM 2100F TEM. After the SSRT test, the surface cracks on the tensile bars were first examined in SEM. For each sample, multiple equally-spaced areas were imaged at fixed magnification across the gage section. Due to the small grain size and crack width, SLMed 304L SS was imaged at a magnification of 5000, and the number of photos is greater than 40. SLMed 304L-1200 SS, 304-A SS and 304-B SS were imaged at a magnification of 1000, and more

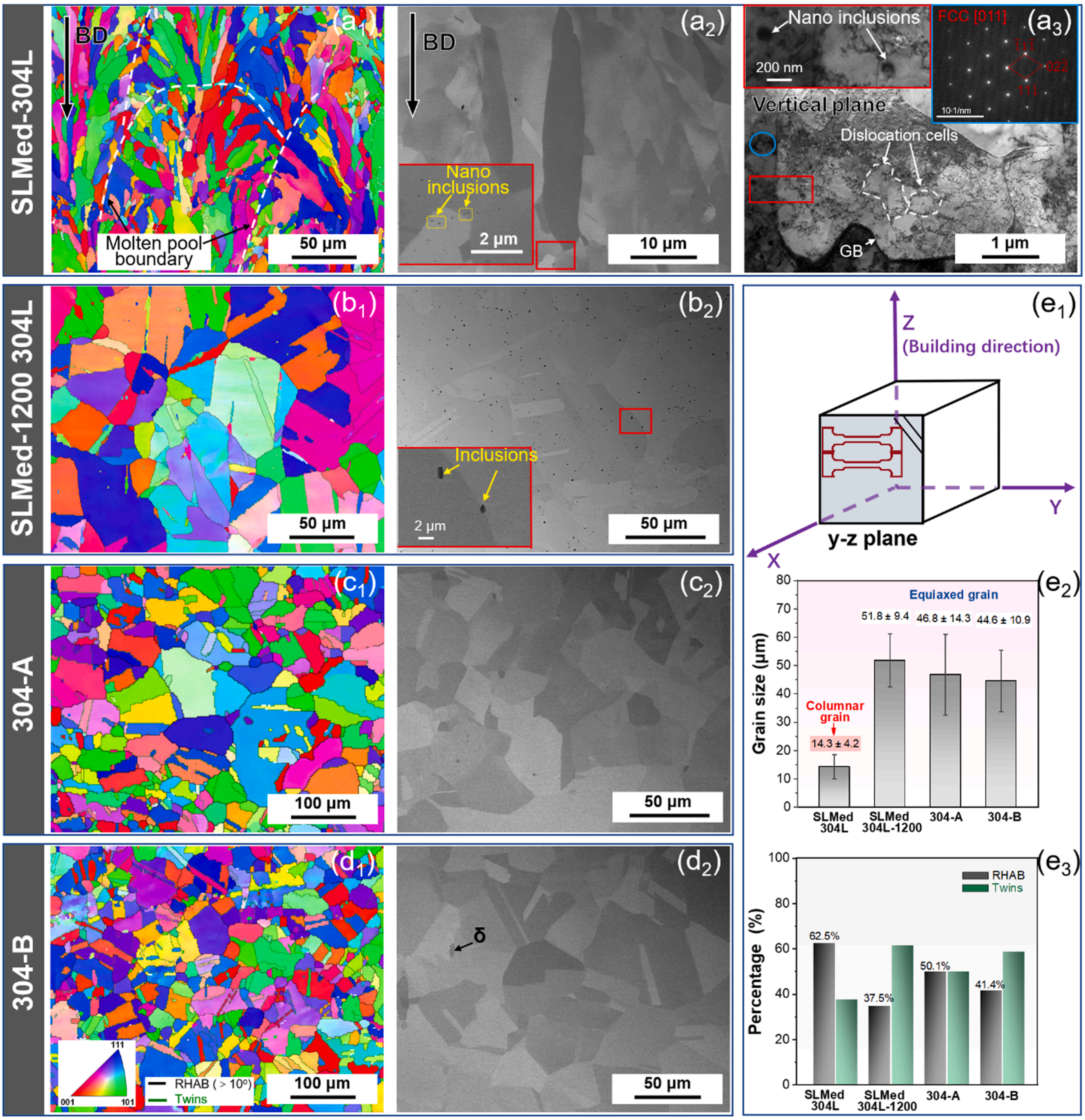

Fig. 1. Microstructure of the (a_1-a_3) SLMed 304L SS, (b_1, b_2) SLMed 304L-1200 SS, (c_1, c_2) 304-A SS and (d_1-d_2) 304-B SS. IPF map of original microstructure of: (a_1) SLMed 304L SS, (b_1) SLMed 304L-1200 SS, (c_1) 304-A SS and (d_1) 304-B SS. The black and grain lines in (a_1, b_1, c_1 and d_1) represent the GBs with a misorientation angle (θ) > 10° and 60° ⟨111⟩ $\sum 3$ twin boundaries, respectively. SEM-BES images of: (a_2) SLMed 304L SS, (b_2) SLMed 304L-1200 SS, (c_2) 304-A SS and (d_2) 304-B SS. Bright-field TEM image of: (a_3) SLMed 304L SS. (e_1) Schematic of the sample orientations relative to the building direction for microstructural characterization and SSRT tests. Bar charter of (e_2) grain size and (e_2) grain boundary character distribution of this four samples.

than 20 images were taken. Crack lengths were measured with self-developed Python based pixel clustering program and the crack number were counted. Crack length per unit area, crack density and average crack length were calculated as in previous works [24,25]. To measure the depths of crack and intergranular oxide, the cross-section samples of tensile bars and corrosion coupons were prepared. Some samples were degreased with acetone and immersed in Ni–P plating solution (the detailed procedure is provided in supplementary materials) at 80 °C for 30 min to form a Ni-P layer for protecting the oxide films and cracks. The samples were mounted in conductive hot resin, ground using SiC papers, and then polished using diamond paste and oxide polishing suspension (OPS) to remove the deformation layer. The FEI Helios NanoLab 600 FIB was also used to extract and prepare electron-transparent lift-out (thinner than 100 nm) from the SSRT specimens for microstructure characterization. The TEM samples were analyzed with a JEOL JEM-200 scanning transmission electron microscope (STEM) equipped with two 100 mm^2 energy dispersive spectroscopy (EDS) detectors and a high angle annular dark-field (HAADF) detector. EDS mapping was acquired by averaging three frames with 512 × 512 pixels with a dwell time of 0.5 μs.

2.5. Strain field measurement

In order to better understand the role of mechanical factor in the process of SCC, high resolution digital image correlation (HR-DIC) was used to evaluate the intrinsic deformation characteristics of SLMed 304L SS and 304-B SS. Two ~1.7 mm-thick tensile samples were prepared. The studied sample surfaces were mechanically abraded up to 2000 grit, electropolished, and finally polished by OPS for 5 min. Both samples were coated with gold for 1 min using a SYSY SBC-12 sputter system. The samples were then placed in hot steam (300 °C) for remodeling the deposited gold layer as in a previous work [26]. After 1.5 h of remodeling, the gold film transforms into speckles pattern (Fig. S1). The gold pattern is at nanoscale, which allows for high resolution strain measurement. Each sample was then strained to ~1.2% at a strain rate of $10^{-4}\ s^{-1}$ at 320 °C. Before and after straining, around 8 sets of images were taken at different magnifications for each sample in the FEI Verios 460 SEM using BSE model with a beam current of 0.2 nA and an accelerating voltage of 5 KV. An open-source 2D DIC software (Ncorr) was used to calculate the local strain field as in previous works [27,28]. To achieve a good tradeoff between resolution and noise, the subset radius and strain radius were set to 10 and 2 pixels, respectively.

3. Results

3.1. Original microstructure characterization

Fig. 1 shows the original microstructures of SLMed 304L SS (Fig. 1a_1-a_3), SLMed 304L-1200 SS (Fig. 1b_1 and b_2), 304-A SS (Fig. 1c_1 and c_2) and 304-B SS (Fig. 1d_1 and d_2) at different scales. The inverse-pole figure (IPF) of SLMed 304L SS (Fig. 1a_1) in this area (250 μm × 200 μm) may contain 3–4 molten pools, which were estimated according to the arrangement of columnar grains. The columnar grains, mostly along the BD, are oriented towards the thermal gradient in perpendicular to molten pool boundary. The width of columnar grain is about 5–15 μm and the length ranges from a few micrometers to about 80 μm. The average grain size is around 14.3 ± 4.2 μm. 62.5% of GB is random high angle grain boundary (RHAB), and the rest is twin boundary (low angle GB is rare and was not counted here). Fig. 1a_2 shows the SEM-BSE image of SLMed 304L SS at high magnification which reveals the distribution of nano inclusions. Nano inclusions are dispersed in the matrix, as shown in the insert in Fig. 1a_2. The TEM bright-field image (Fig. 1a_3) shows a tiny local area containing GB, dislocation cells and nano inclusions. The selected area electron diffraction (SAED) taken from the light blue circled area shows that the matrix is face-centered cubic austenite structure. The EDS analysis (supplementary material, Fig. S2) in the

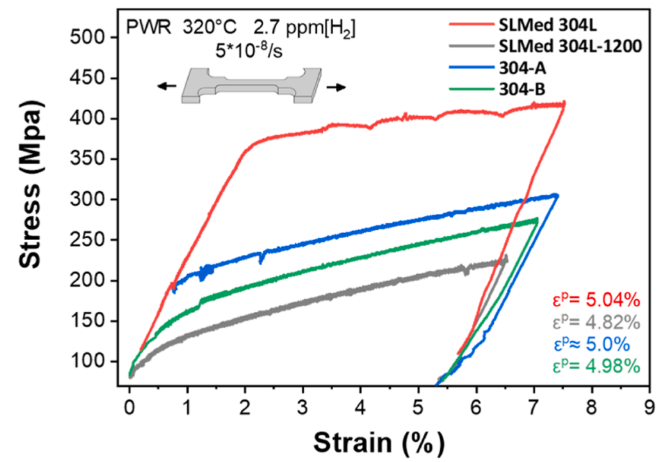

Fig. 2. Stress-strain curves of SLMed 304 L SS, SLMed 304L-1200 SS, 304-A SS and 304-B SS samples strained at 5×10^{-8} /s in 320 °C water containing 2.7 ppm hydrogen.

STEM shows that the nano inclusion contains 41.5% Fe, 28.4% O, 18.0% Cr, 5.9% Ni, 0.6% Mo and 5.5% Si (atomic percent), confirming that it is an oxide inclusion slightly enriched in Si. From the local enlarged image in Fig. 1a_3, the diameter of inclusion is about 100 nm. High concentration of dislocations forms dense dislocation cells in some grain. The dislocation density is non-uniform as some grains have lower concentration of dislocations and almost no dislocation cell. Fig. 1b_1 and b_2 show the microstructure of SLMed 304L-1200 SS. After heat treatment at 1200 °C, the nonequilibrium microstructure of the SLMed 304L SS was fully recrystallized. With the vanish of prior structure, the grains grow (from 14.3 ± 4.2 to 51.8 ± 9.4 μm) and become equiaxed. The length fraction of RHABs is 34.9% and that of twin boundaries is 65.1% (Fig. 1b_1). The size of inclusions also increased from ~100 nm to ~3 μm. The inclusions are distributed both inside the grains and along the GBs. The SEM-EDS analysis (supplementary material, Fig. S3) indicates that the inclusion is Cr-rich oxide and also contains some carbon.

The microstructures of forged 304-A SS and 304-B SS are shown in Fig. 1c_1-d_3. The two materials display typical annealed microstructure consisting of equiaxed grains with the average grain size of 46.8 ± 14.3 μm and 44.6 ± 10.9 μm (Fig. 1c_1 and d_1). 304-B SS has more uniform grain size and regular grain shape. 304-A SS and 304-B SS contain 50.1% and 58.6% twin boundaries, respectively. SEM-BSE images (Fig. 1c_2 and d_2) indicate that there is no obvious precipitate in the two materials, and 304-B SS has some δ ferrite islands in the matrix of austenite. Fig. 1e_1 shows the sampling directions of SLMed 304L SS and SLMed 304L-1200 SS relevant to the BD in present study. The grain size and proportion of GB type are plotted in Fig. 1e_2 and e_3. The grain size of SLMed 304L SS is the smallest, while those of the other three SSs are comparable (Fig. 1e_2). SLMed 304 L SS has the highest proportion of RHAB, while after annealing at 1200 °C, the proportion of RHAB decreases to the lowest value among the four SSs.

3.2. SSRT test

Fig. 2 shows the stress-strain curves of the four materials (the preloading curve of 304-A is missing because the recorded data was lost) acquired during the SSRT test. The yield strength of SLMed 304L SS at 320 °C (370 MPa) is higher than those of two wrought SS (304-A is about 150 MPa and 304-B is 125 MPa). However, SLMed 304L-1200 SS, 304-A SS and 304-B SS show stronger working hardening ability than SLMed 304L SS. At the end of SSRT test, the real plastic strains of this four SS samples were measured to be 5.04%, 4.82%, ~5% and 4.98%, and the final stresses reached 415, 231, 305 and 274 MPa, respectively (Table 2).

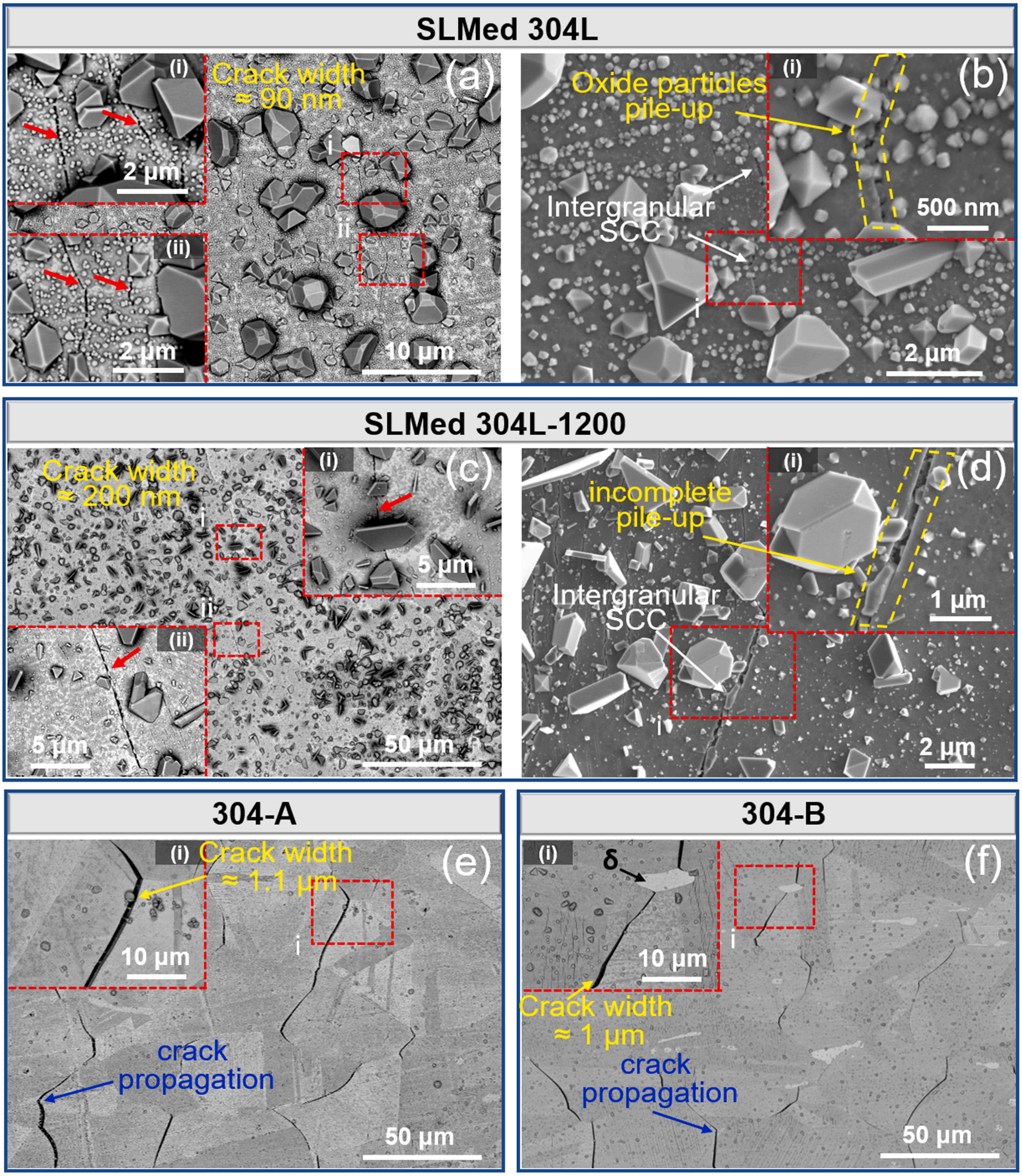

Fig. 3. (a) SEM-BSE image, (b) SEM-SE image of the gage section of the SLMed 304L SS sample after SSRT test, (c) SEM-BSE image, (d) SEM-SE image of the gage section of the SLMed 304L-1200 SS sample after SSRT test, SEM-BSE images of (e) 304-A SS and (f) 304-B SS of gage section after SSRT tests, (all the tensile direction is aligned the horizontal direction).

3.3. Post-SSRT test characterization

3.3.1. Plan-view evaluation of SSRT samples

The plan-view SEM images of SSRT samples are shown in Fig. 3a-f, and the SCC test conditions and results are summarized in Table 2. The length and number of the cracked GBs were measured separately on each sample. As shown in Fig. 3a, the oxide particles on the surface of SLMed 304L SS are faceted and vary in size from about 4 μm to several hundred nanometers. From the high magnification image (Fig. 3a), the cracked GBs is mostly perpendicular to the tensile direction. Fig. 3b reveals that the cracks are narrow (with width less than 100 nm) and filled with many small oxide particles.

The SEM-BSE and SEM-SE images of SLMed 304L-1200 SS are showed in Fig. 3c and d. It can be seen from Fig. 3c that the number density of cracked GBs is lower in SLMed 304L-1200 SS, but the cracks are longer and wider than that of SLMed 304L SS (Fig. 3a). Fig. 3d shows the detailed morphology of the cracked GB on SLMed 304L-1200 SS. The oxide particles partially block the crack mouth, and the small oxide particles are less dense than those on SLMed 304 L SS (Fig. 3b).

Fig. 3e and f show the surfaces of 304-A SS and 304-B SS. The crack and oxide morphologies in these two materials are different from the previous two samples (Fig. 3a-d): the oxide particles on the outer layer are sparse and the intergranular cracks are longer and wider. These longer cracks already passed the initiation stage and propagated to the adjacent GBs, resulting in increased crack length and opening (Fig. 3e and f). However, when some of the intergranular cracks in 304-B SS encounter the δ ferrite (indicated by black arrows in Fig. 3f), the propagations are hindered and the cracks get narrow or interrupted, as shown in the inset in Fig. 3f. The cracking of two wrought 304 SSs in this work seems more severe than those reported from the previous researches [29,30]. Relevant data from Chang et al. [29] suggests that the annealed SS is quite resistant to SCC initiation. Such difference in SCC resistance is probably caused by the difference in experimental condition or chemical composition of tested material among different laboratories.

The average crack length, crack density, crack length per unit area, GB length density and percentage of cracked GB for each sample are listed in Table 2. SLMed 304L SS has the highest crack density and crack length per unit area, followed by 304-B SS and SLMed 304L-1200 SS, and finally 304-A SS. It should be noted that SLMed 304L SS has the

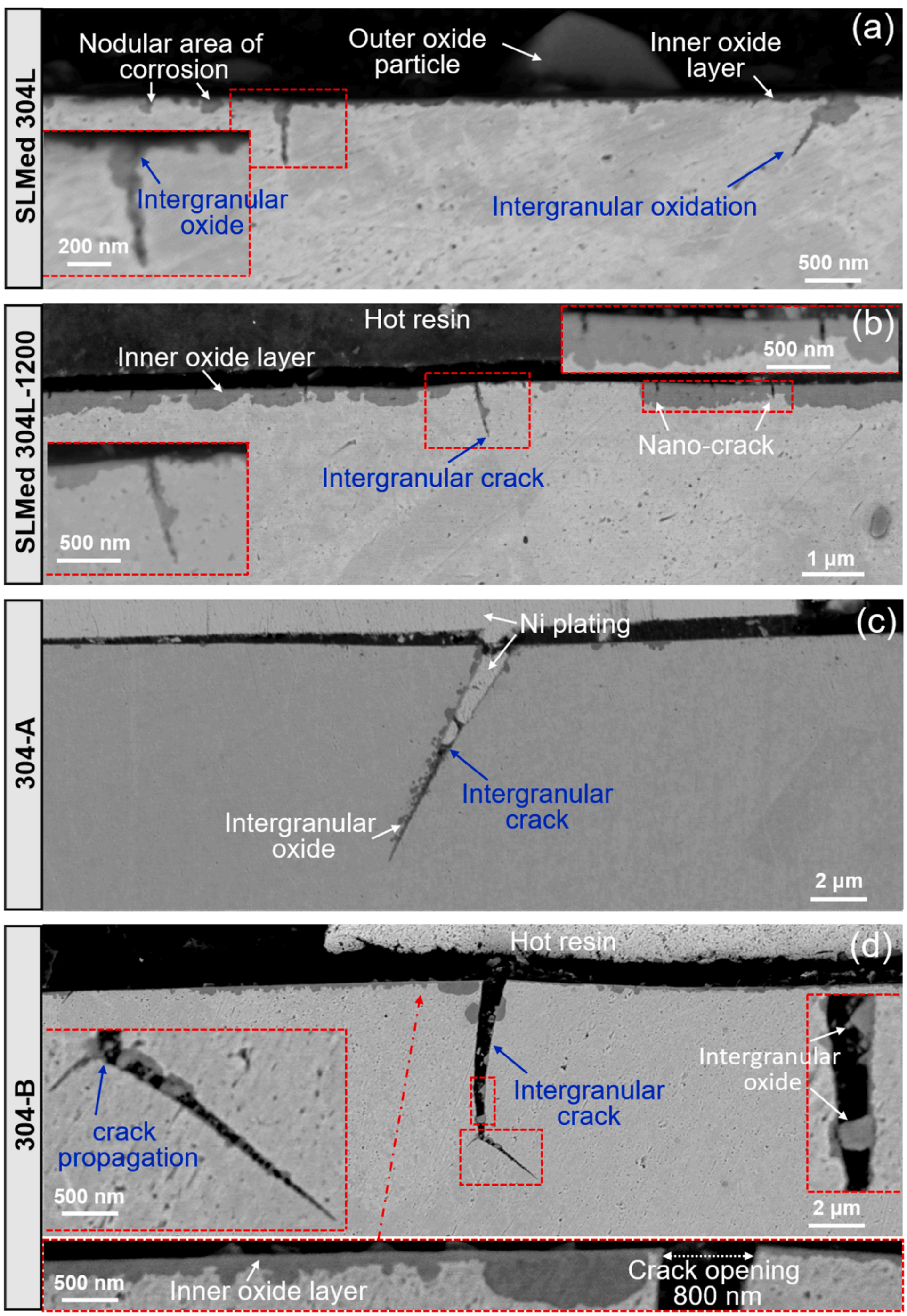

Fig. 4. SEM-BSE image of the cracks obtained from the cross-section of the SSRT samples of the (a) SLMed 304L SS, (b) SLMed 304L-1200 SS, (c) 304-A SS and (d) 304-B SS.

highest GB length density because its grain size is about one third of those of the other three materials. The crack length per unit area is usually used as a comprehensive parameter to evaluate the susceptibility to SCC initiation [24,25,31]. However, since the crack length per unit area is highly dependent on the original GB length density, this parameter could not be directly used to reflect the difference in SCC susceptibility between materials with drastically different grain sizes. Therefore, the percentage of GB cracking, which is the crack length per unit area divided by GB density, is used here. The results show that SLMed 304L SS has the lowest percentage of cracked GB, while SLMed 304L-1200 SS and 304-B SS show the highest percentages.

3.3.2. Cross-section characterization of SSRT samples

To further evaluate the SCC susceptibility of different materials, tensile specimens were sectioned longitudinally and examined to determine the extent of intergranular cracking. Fig. 4a-d show the SEM-BSE images of the cross-section samples. From Fig. 4a, the surface of SLMed 304L SS is covered by a typical double-layer oxide and intergranular oxidation occurs. The inner oxide is continuous and nodular corrosion occurs in some area (Fig. 4a). The formation of nodular oxide in SSs in PWR water environment can also been found in previous works [32–35]. The thickness of the inner layer is about 100 nm. Below the inner oxide layer, extremely narrow and shallow intergranular oxidation is observed. As the intergranular crack is very shallow and filled with oxide particles, cracking gap can't be clearly identified on the cross section. Fig. 4b shows the cross section of SLMed 304L SS-1200 SS. According to Fig. 4a and b, the inner oxide layer of SLMed 304L-1200 SS is thicker than that of SLMed 304L SS. Some small cracks (indicated by white arrows on the right in Fig. 4b) are located in the inner oxide layer with a depth of 100–200 nm. In addition, the intergranular crack is within the intergranular oxide and the cracking gap is very narrow. The intergranular oxidation penetration is deeper than that of the SLMed 304L SS.

Cracks in 304-A SS and 304-B SS are mainly along GBs and normally propagate deeper, as shown in Fig. 4c and d. The crack tips of these two SSs are very sharp with wider cracking opening (Fig. 4c and d). Additionally, intergranular oxide can be observed beyond the intergranular crack in Fig. 4c. Fig. 4d shows a wider intergranular crack propagating into a GB triple junction which is partly filled with oxide particles. Therefore, compared with SLMed 304L SS and SLMed 304L-1200 SS, the intergranular cracks of 304-A SS and 304-B SS are deeper, wider and filled with fewer oxidation product.

The crack tips from the tensile samples were further examined at higher magnification in SEM-BSE mode. After checking dozens of crack tips for each sample, it is found that GB migration zone formed beyond the crack tips along some GBs in SLMed 304L SS and SLMed 304L-1200 SS (as shown in Fig. 5a and b), but none was observed in 304-A SS and 304-B SS (not show here). The GB migration zone of SLMed 304L SS (the length is about 100 nm) appear brighter due to its higher Ni content than the surrounding matrix (as shown in the red dashed box in Fig. 5a).

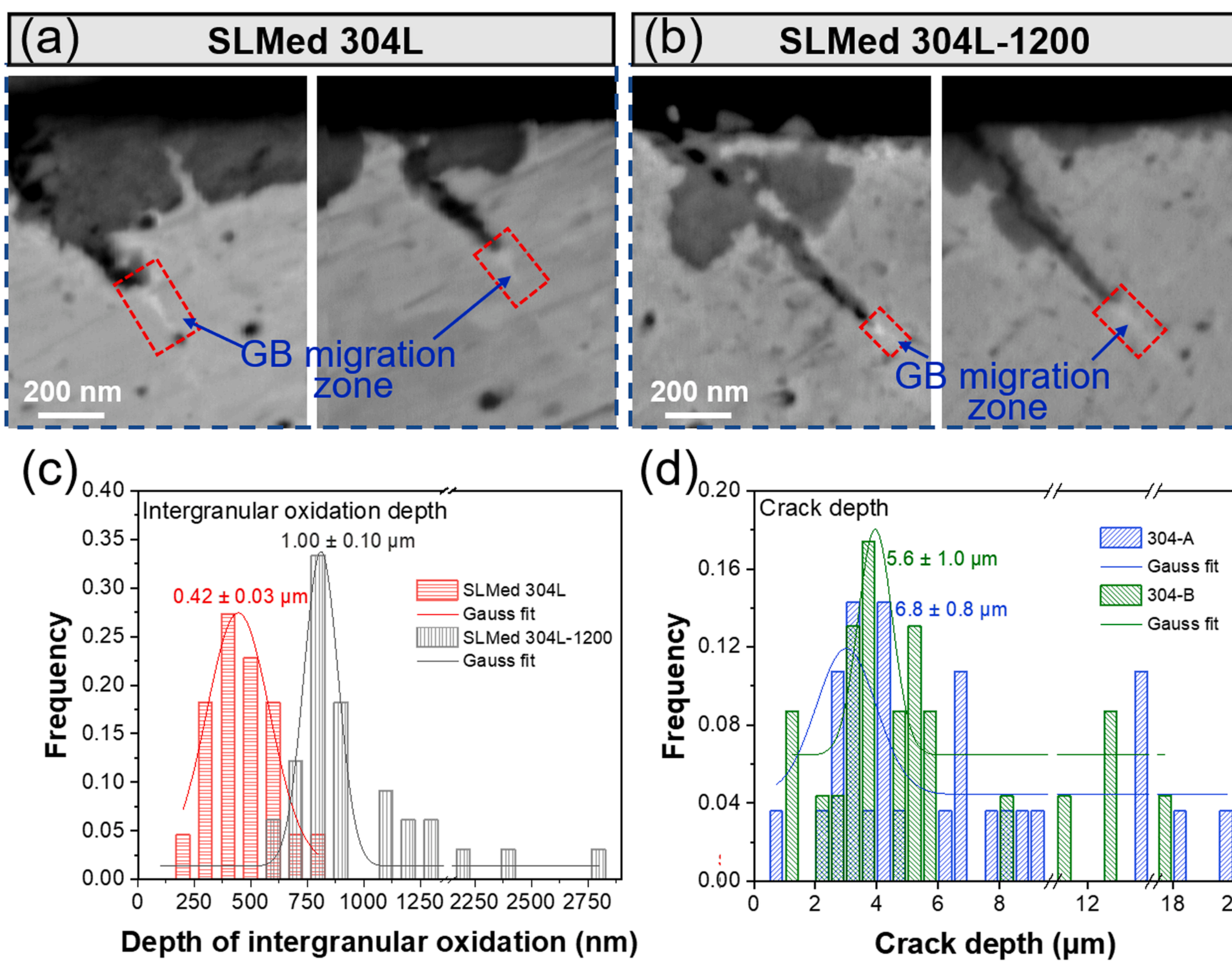

Fig. 5. SEM-BSE images of GB migration zone in (a) SLMed 304L SS and (b) SLMed 304L-1200 SS SSRT samples. (c) Depth measurement of the intergranular oxidation of SLMed 304L SS and SLMed 304L-1200 SS SSRT samples (The number of oxidized GB samples per SS sample exceeds 21), (d) Crack length measurement of the intergranular crack of 304-A SS and 304-B SS SSRT samples (The number of cracked GB samples per SS sample exceeds 28). The uncertainty of the sample mean value uses the standard error of mean.

Then, the depth of intergranular cracking was measured to evaluate the SCC susceptibility of materials. Given that the cracks on SLMed 304L SS and SLMed 304L-1200 SS are very shallow and always filled with oxide particles, they could not be easily differentiated from oxidized GB (Fig. 4a and b). Therefore, the depth of penetrative intergranular oxidation was measured from these two samples to reflect the upper limit of crack depth. The number of sampled GBs is greater than 21. The depth of intergranular oxidation of SLMed 304L SS is significantly smaller (0.42 ± 0.03 μm) than that of SLMed 304L-1200 SS (1.00 ± 0.10 μm), as can be seen from the bar chart in Fig. 5c. This result is in agreement with the plan-view observation that SLMed 304L SS has shorter crack length and narrower crack opening. The numbers of measured GBs from 304-A SS and 304-B SS SSRT samples are 28 and 37, respectively. As shown in Fig. 5d, the depth of intergranular crack from these two samples ranges from 0.8 to 19.8 μm, with an average depth of 6.8 ± 0.8 μm for 304-A SS and 5.6 ± 1.0 μm for 304-B SS. The results suggest that SLMed 304L SS and SLMed 304L-1200 SS perform better than the wrought SSs in SCC initiation and SLMed 304L SS exhibits the highest resistance.

3.4. Characterization of corrosion coupon

The un-stressed coupons are further analyzed to assess the intergranular oxidation resistances of different samples. Fig. 6 shows the SEM-BSE images of the cross-sections of the four samples. Intergranular oxidation has occurred on all the samples (as denoted by the blue arrows in Fig. 6). As shown in Fig. 6a, the intergranular oxidation in SLMed 304L SS is very shallow. It can be seen from Fig. 6b that SLMed 304L-1200 SS has a thicker inner oxide layer with obvious intergranular oxidation. Fig. 6c shows typical intergranular oxidation in 304-A SS, which is very narrow and penetrates deeper along the GB. The inner oxide layer is very thin with some small areas of nodular oxidation. 304-B SS also shows long and narrow intergranular oxidation as 304-A SS (Fig. 6d).

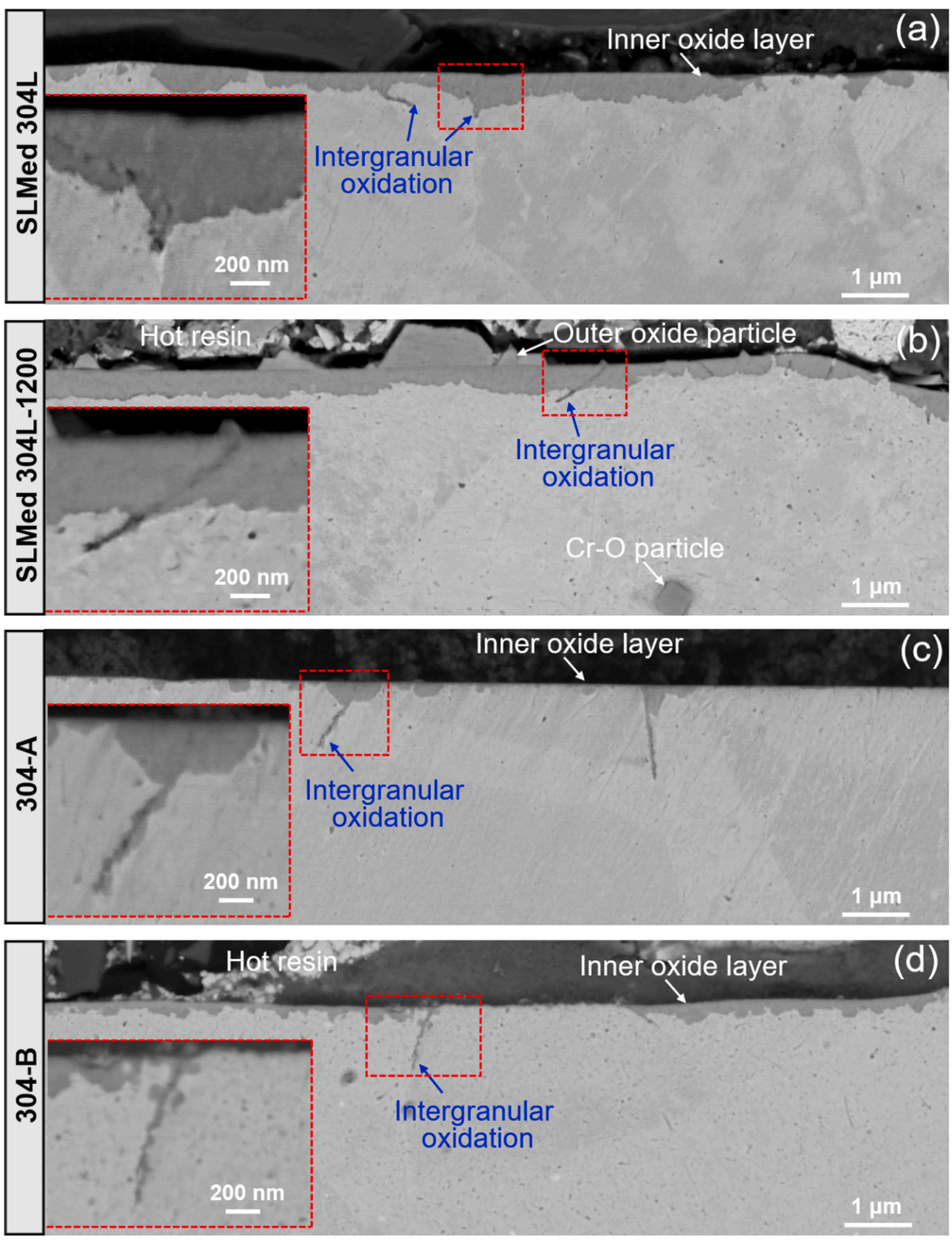

Fig. 6. SEM-BSE image of the intergranular oxidation obtained from the cross-section of corrosion coupons sample of the (a) SLMed 304L SS, (b) SLMed 304L-1200 SS, (c) 304-A SS and (d) 304-B SS, all the samples were employed for the exposure tests with a fixed exposure period of 622 h.

The depths of intergranular oxidation of four coupons are summarized in the bar charts in Fig. 7. To ensure the statistical significance, the number of measured oxidized GBs for each sample is greater than 35. Specifically, the depth of intergranular oxidation is 1.20 ± 0.05 μm for 304-A SS and 1.40 ± 0.12 μm for 304-B SS. Compared with the above two wrought SS, the depth of intergranular oxidation for other two samples is shorter, which is 0.59 ± 0.03 μm for SLMed 304L SS and 0.75 ± 0.03 μm for SLMed 304L-1200 SS.

3.5. Microstructure analysis of crack

In this section, microstructure characterization was performed on an electron-transparent FIB lift-out extracted from a cracked GB of SLMed 304L SS to further study the microstructural features. Fig. 8a shows the SEM-SE image of the sampled crack which has an opening of ~200 nm. From the STEM-HAADF image of the cross section (Fig. 8b) and the enlarged image from the selected area of Fig. 8b (Fig. 8c), the crack wall is covered with a thick oxide layer. The oxide on the sample surface has a typical double-layer structure consisting of an outer layer of discrete oxide particles and a continuous inner oxide layer. The intergranular oxidation depth within this crack is about 960 nm, which is much deeper than the average depth of the cracks from SLMed SS (Fig. 5c). The crack tip is located in the middle of intergranular oxide with a depth of about 430 nm (Fig. 8b and c), which is much shorter than that of 304-A SS and 304-B SS samples (Fig. 4f). In addition, the intergranular oxide is not uniform but contains two distinct regions which are denoted as A and B (Fig. 8c). Region A is located in the middle and upper part of the intergranular oxide. Region B is on the bottom of intergranular oxide and contains concentrated pores. There are fine pores distributed at the metal/oxide interface. Additionally, the GB migration zone is observed beyond the intergranular oxide (as indicated by black dotted line).

STEM-EDS mappings of the same area in Fig. 8b are shown in Fig. 8d-g. From the O mapping (Fig. 8d), the crack gap can be easily identified as it is depleted in O. The inner oxide on the surface and most of the intergranular oxide are depleted in Fe and Ni and contain similar Cr content as the matrix (Fig. 8e-g). In contrast, region A is depleted in Cr and contains significant Fe as the outer oxide particles which are formed by dissolution-precipitation mechanism [36]. Thus, it is believed that the oxide in region A is also formed by precipitation. As for region B, the intergranular oxide shows composition similar to the inner oxide layer. As such, the oxide in region B should be formed via the inward diffusion of oxygen. Beyond the oxide, a Ni-enriched and Cr-depleted GB migration zone formed. The GB migration in austenitic SS has also been reported before [34].

The intergranular oxide and GB migration zone are enlarged in Fig. 9a. The GB migration zone starts at the tip of the intergranular oxide and extends for around 370 nm along the GB. The migration zone is surrounded by the straight original GB (on the right) and the curved migrated GB (on the left). STEM-EDS mappings in Fig. 9b show elemental distribution of Fig. 9a. The tip of the intergranular oxide is slightly enriched in Cr, and depleted in Fe and Ni (Fig. 9b). The GB migration zone beyond the intergranular oxide is enriched in Ni and depleted in Cr and Fe (Fig. 9b). The Cr-enriched oxide penetrates into the GB migration zone (Fig. 9b), as have been reported in alloy 690 [27, 37]. In order to trace the element contents across the attacked GB, EDS line scans were taken along the arrows in Fig. 9a and shown in Fig. 9c and d. The line profiles confirm that the intergranular oxide is Cr-enriched and the Ni content in GB migration zone is as high as 70 at.% with concomitant depletions of Fe and Cr (depleted to 26 at.% and 5 at.%, respectively).

3.6. Strain field analysis

HR-DIC was used to carefully characterize the slip behavior of materials. The HR-DIC strain maps along tensile direction following a macroscopic plastic straining of ~1.2% is shown in Fig. 10. The average normal strains (ε_{xx}) of both samples are ~1.3% (the sampled area is ~180×120 μm^2). Fig. S4(a, b) shows the effective shear strain (γ_{eff}) maps of the same region of Fig. 10 (the detailed procedure of calculating 2D shear strain is provided in Supplementary materials). 304-B SS shows evident parallel planar slip bands in almost every grain (Fig. 10b$_1$, b$_2$) while SLMed 304L SS only exhibits scattered slip bands in some grains (Fig. 10a$_1$, a$_2$). Fig. 10c shows the distribution of normalized ε_{xx} (normalized by the average normal strain of sampled area) at an interval size of 0.001 for the two SSs. The distribution of normalized ε_{xx} in 304-B SS is slightly more heterogeneous than that in SLMed 304L SS (the distribution of γ_{eff} shows the same trend (Fig. S4c)). The frequency of high normalized strain is higher in 304-B SS due to the presence of larger number of slip bands. To better reveal the highly-strained area, a minimum threshold normalized ε_{xx} of 1.2 was applied and the maps are shown as insets in Fig. 10c. There are only 58–65 highly strained slip bands in the SLMed 304L SS while 304-B SS shows about 152 bands.

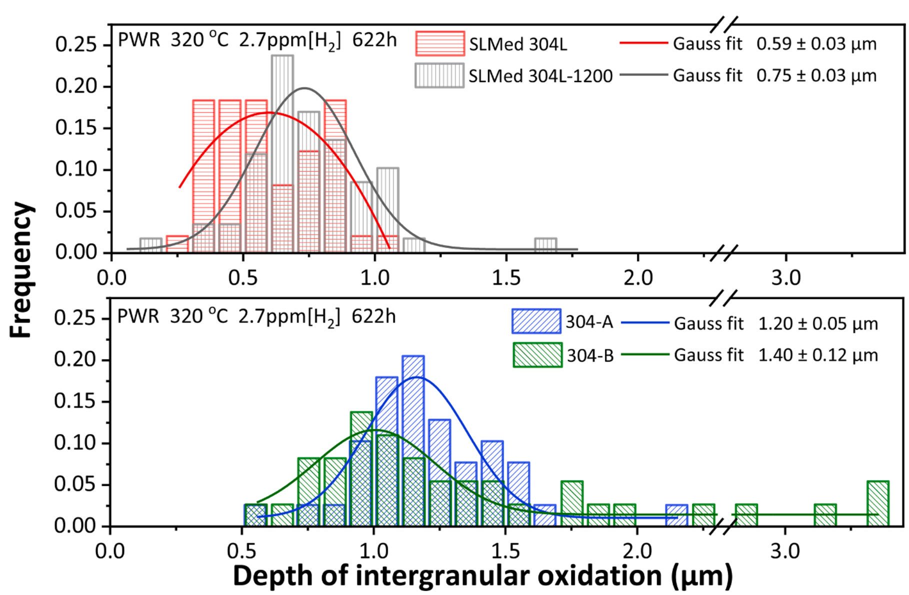

Fig. 7. Depth distribution of the intergranular oxidation of SLMed 304L SS, SLMed 304L-1200 SS, 304-A SS and 304-B SS (The number of measured oxidized GBs per SS sample exceeds 35). The uncertainty of the sample mean value uses the standard error of mean.

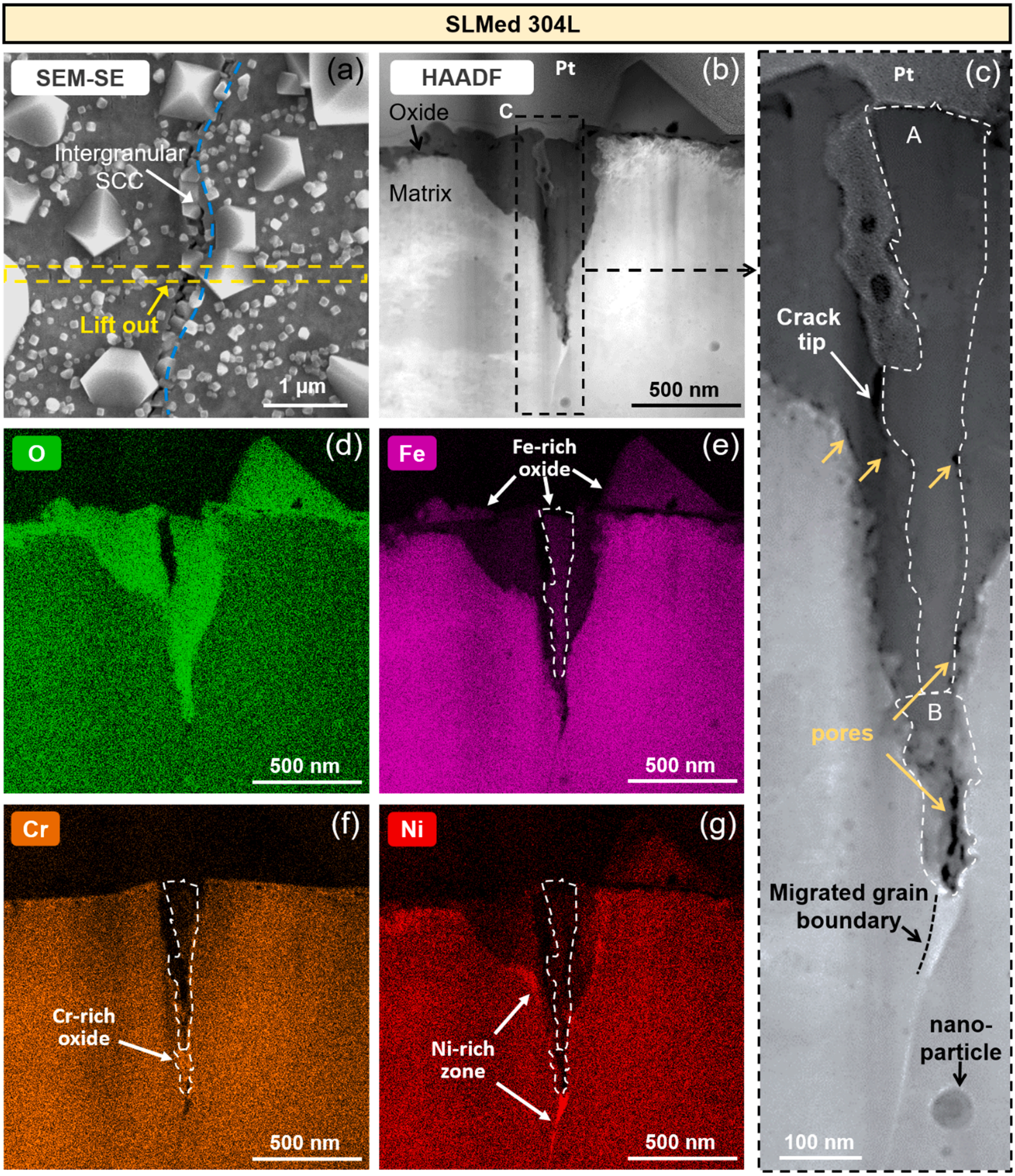

Fig. 8. (a) SEM-SE image of a intergranular crack on SLMed 304L SS, strained to 5.04% at $5 \times 10^{-8}\ s^{-1}$ in high purity water containing 2.7 ppm H_2. (b) STEM-HAADF image of the crack cross-section. (c) Enlarged image of the framed area in image b (some pores are indicated by light-yellow arrows). EDS mappings of (d) O, (e) Fe, (f) Cr and (g) Ni of image b.

Thus, the degree of planar slip is greater in 304-B SS compared to SLMed 304L SS.

4. Discussion

The SCC results show that the SLMed 304L SS has much higher resistance than that of the wrought 304 SS. The percentage of cracked GBs and the depth of intergranular cracks are used as indicators to evaluate the SCC susceptibility, as shown in Table 3 and plotted in Fig. 11. For the first time, these results indicate that SLMed 304L SS has much higher resistance to SCC initiation than the traditional wrought SSs, which is an exciting discovery to the additive manufacturing community. Three additional SLMed 304L SS samples cut from other orientations and another nuclear grade wrought 304 SS were also tested and the experimental results are consistent with those presented in this paper.

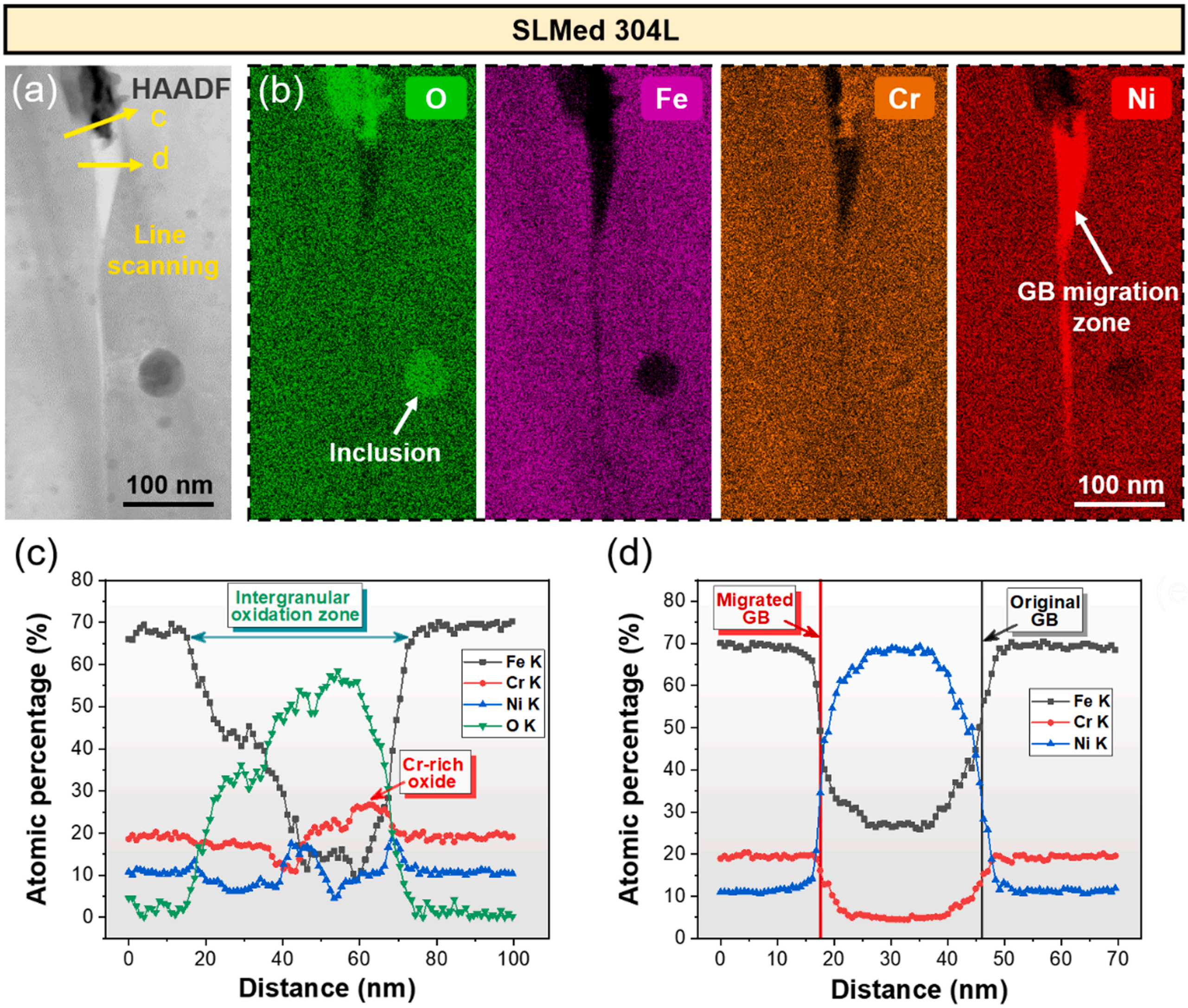

Fig. 9. (a) STEM-HAADF image of GB migration zone of SLMed 304L SS, (b) EDS mapping of O, Fe, Cr and Ni of image a, (c) and (d) STEM-EDS line profiles along line c and d in a.

The SCC of materials is a synergistic process between chemical (corrosion) and mechanical behaviors which is highly dependent on the chemical composition and microstructure of material. Tracking the cause of the differences in SCC susceptibility between the SLMed 304L SS and the wrought 304 SS is challenging as both the composition and microstructure are quite different between them (Table 3). Thus, SLMed 304L-1200 was introduced here as an intermediate to better separate the effects of chemical composition and microstructure on SCC. These effects will be discussed from the aspects of intergranular oxidation and dislocation slip mode.

4.1. The effects of chemical composition on SCC initiation

In order to single out the effect of chemical composition on SCC susceptibility, the wrought SSs are compared with SLMed 304L-1200 SS which has a similar equiaxed grain structure. From Fig. 11, SLMed 304L-1200 SS has a much shallower crack depth than the two wrought SSs, suggesting that it exhibits higher resistance to SCC initiation. Given that these three materials have similar grain structures, the differences in SCC resistance should mainly result from the different chemical compositions. Now increasing data indicates that intergranular oxidation is a necessary precursor for SCC initiation [34,37-41]. The SCC resistance should be closely related to the oxidation rate of GB. From Fig. 7, the depth of intergranular oxidation measured from SLMed 304L-1200 SS is smaller than those from the wrought SSs (0.75 ± 0.03 μm vs 1.20 ± 0.05 μm and 1.40 ± 0.12 μm), consistent with the fact that SLMed 304L-1200 SS has higher resistance to SCC initiation than the wrought SSs. The primary effect of chemical composition on the SCC resistance can be understood from its role in the GB oxidation behavior [42].

In this study, there is significant difference in chemical composition between the SLMed SS and the two wrought 304 SSs (Table 1). 304-A SS and 304-B SS have similar compositions with contents of Si and Mn one order of magnitude higher than those in SLMed SS. Si is a common impurity in SS and is typically a high-concentration impurity in LWRs water (20–1000 ppb) since it can be easily oxidized to SiO_2 which is highly soluble in high temperature water [43]. The high content of Si would have a negative effect on the oxidation and cracking resistances of GBs [44–46]. Now increasing researches suggest that Si is detrimental to the SCC resistance of material in high temperature water. Andresen and Morra [43] found that Si could increase SCC CGRs of 304L SSs in hydrogenated water chemistry (HWC) significantly. Li et al. [45] also reported that elevated Si content could promote the SCC CGR of 12% Cr-28% Ni SS in PWR primary water. They proposed three possible effects of Si, namely, reducing the stacking faults energy, decreasing the strength of oxide film and increasing intergranular oxidation tendency of GBs. The Si effect is also highly concerned in the SCC of irradiated

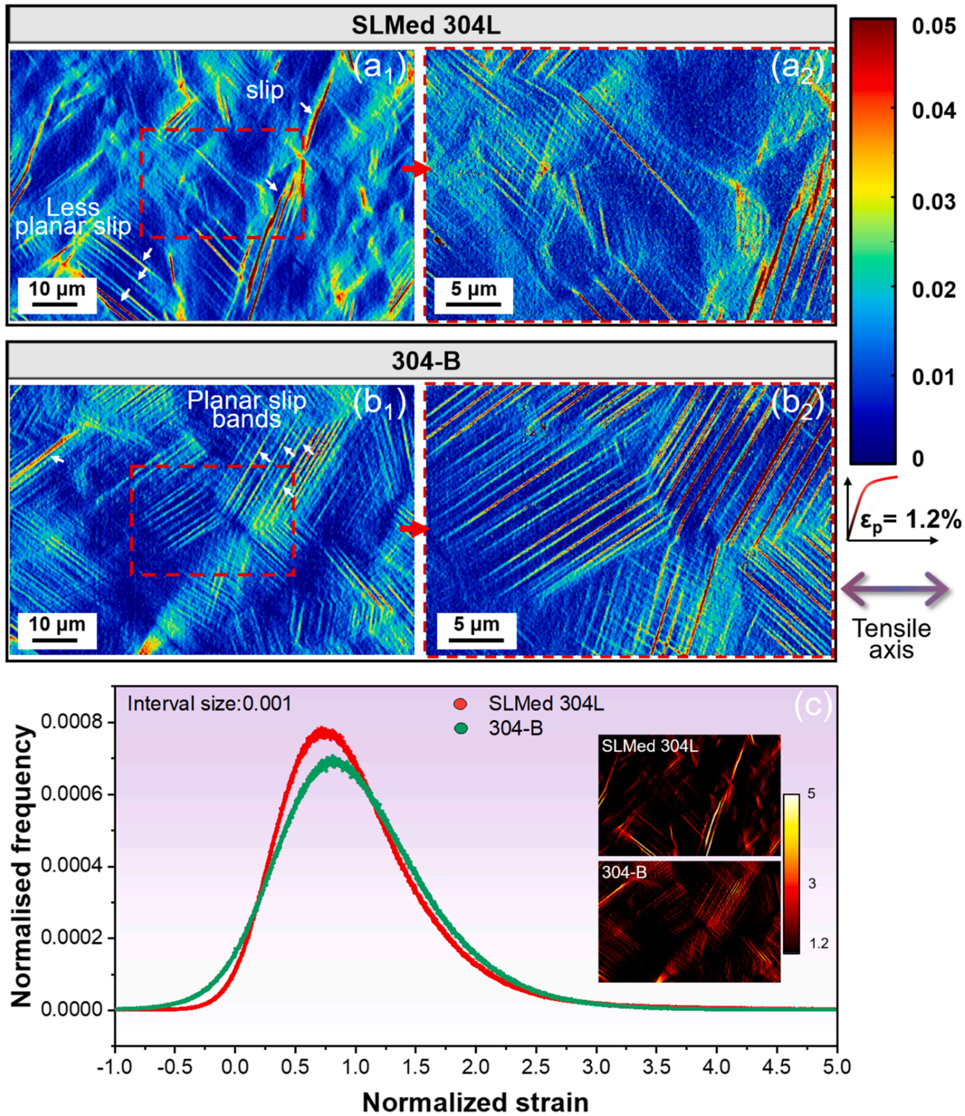

Fig. 10. Strain field distribution of normal strain ε_{xx} from HR-DIC data at ~1.2% macroscopic plastic strain of SLMed 304 L SS (a_1, a_2) and 304-B SS (b_1, b_2). (c) Normalized frequency distribution of normal strain ε_{xx} (the average ε_{xx} of SLMed 304 L SS and 304-B is 0.0136 and 0.0131, respectively).

Table 3
Summary of characteristics of four SS samples.

Variants		Samples			
		SLMed 304L	SLMed 304L-1200	304-A	304-B
Chemical composition		Si-Mn free, Mo 0.83 wt.%		Contain Si and Mn	
Microstructure	Molten pool	√	×	×	×
	Grain	Columnar	Equiaxed	Equiaxed	Equiaxed
	Inclusion	Nano-scale	Micro-scale	×	×
	Dislocation cell	√	×	×	×
SCC susceptibility	Plan-view (%)	11.43 ± 0.78	30.13 ± 0.56	19.51 ± 0.54	28.33 ± 0.28
	Cross-section (µm)	0.42 ± 0.03	1.00 ± 0.10	6.8 ± 0.8	5.6 ± 1.0
Intergranular oxidation	Cross-section (µm)	0.59 ± 0.03	0.75 ± 0.03	1.20 ± 0.05	1.40 ± 0.12
DIC strain analysis		Less planar slip			Planar slip

√: It has this characteristic. ×: There is no such characteristic.

materials as Si segregates at GBs during irradiation. Kuang et al. [46] reported that post-irradiation annealing treatments could decrease the SCC CGR of neutron-irradiated 304L SS in HWC water and linked it to the recovery of Si segregation. Recently, they studied the microstructure features of SCC cracks from a proton-irradiated 316L SS and revealed that Si segregated at GB tends to get oxidized preferentially and then dissolves into solution. Similar result has been reported in neutron-irradiated SS [47]. The dissolution of Si-rich oxide leads to a porous intergranular oxide which would make an easy path for further oxidation and cracking. The enhanced intergranular oxidation rate of the wrought SSs compared to SLMed 304L-1200 SS probably results from their higher Si contents. Thus, Si, especially when segregated at

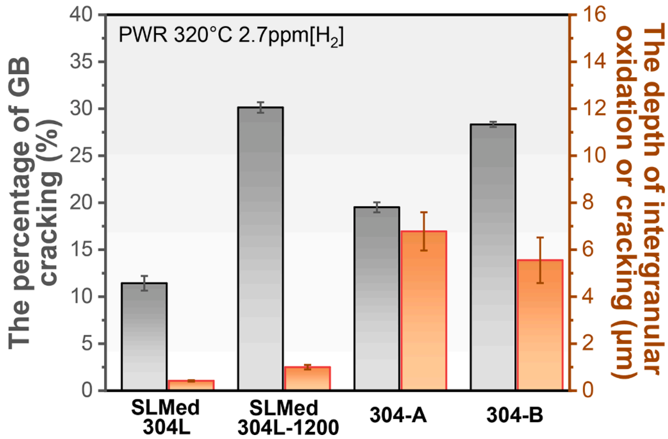

Fig. 11. SCC susceptibility of SLMed 304L SS, SLMed 304L-1200 SS, 304-A SS and 304-B SS evaluated from plan-view and cross-section characterizations.

GB, is detrimental to the SCC resistance of SS in high temperature water as it enhances the tendency to intergranular oxidation.

Mn probably has a similar effect on oxidation as Si. Recent work by Dong et al. [48] shows that multi-component alloy FeCrNiMn exhibits extensive intergranular cracking after SSRT test in PWR water. It was suggested that Mn has the highest affinity to oxygen among these four elements and the oxidized Mn tends to dissolve into solution, making the formed oxide layer porous. In summary, compared to the wrought SSs, SLMed 304L-1200 SS has higher resistance to intergranular oxidation and cracking thanks to its lower contents of Si and Mn.

In addition, the wrought 304 SSs contain much lower contents of Mo than SLMed 304L-1200 SS (0.22 wt.% vs 0.83 wt.%). Mo may be beneficial to oxidation resistance. Although there are few reports on the role of Mo in LWR environment, massive data reveals that minor Mo addition has pronounced effects on the localized corrosion of alloys containing Cr [49–52]. TEM in-situ oxidation of Fe-Cr-Mo alloy shows that Mo can inhibit the mobility of metal cation vacancies and help to prevent the formation of Kirkendall voids [51]. Mo may also play a role in improving the corrosion properties of SLMed 304L-1200 SS. The Mo in the GBs of SLMed 304L-1200 SS can stabilize the protective oxide film.

Therefore, SLMed 304L-1200 SS possesses higher intergranular oxidation and SCC initiation resistances than the wrought 304 SS in hydrogenated high temperature water due to its optimized chemical composition, i.e. reduced contents of Si and Mn, and doped with Mo.

4.2. The effect of microstructure on SCC initiation

The unique microstructure of SLMed 304L SS has significant effects on the corrosion and mechanical behaviors of material, and hence affects the SCC initiation susceptibility. SLMed 304L SS has multi-scale microstructures, including molten pools, columnar grains, dense dislocation cells and amorphous nano oxide inclusions (Table 3). In contrast, SLMed 304L-1200 SS and the two wrought SSs have typical equiaxed grain microstructure. The effect of microstructure on the SCC resistance can be easily revealed by comparing SLMed 304L SS with SLMed 304L-1200 SS as both have the same composition. Fig. 5 clearly shows that SLMed 304L SS indeed has higher resistance to SCC initiation than SLMed 304L-1200 SS, indicating that the unique microstructures induced by printing clearly enhance the SCC resistance.

The effect of columnar grain structure on the SCC resistance should be considered. The AM material normally exhibits higher resistance to SCC when loaded along BD than when loaded perpendicular to BD. That is because the normal stress on most GBs, which is the driving force for SCC, is much lower when loaded along BD. Lou et al. [12] found that the longitudinal GB of columnar grain is a preferential pathway of SCC growth for stress-relieved SLM 316L SS in both NWC and HWC water. In this work, for SLMed 304L SS, the longitudinal direction of columnar grains (i.e. BD) is perpendicular to the tensile direction (Fig. 3a and b). As such, more GBs should be subjected to high normal stress in SLMed 304L SS compared to other equiaxed SSs. Although SLMed 304L SS is under an unfavorable loading condition, it still exhibits much lower SCC tendency than SLMed 304L-1200 SS. Therefore, the superior SCC performance of SLMed 304L SS should be attributed to other microstructure features, i.e. dislocation cells and oxide inclusions. The effects of these features on the SCC resistance will be discussed from their roles in the intergranular oxidation and dislocation slip behavior.

4.2.1. Effect of microstructure on the intergranular oxidation behavior

The intergranular oxidation depth of SLMed 304L SS is lower than that of SLMed 304L-1200 SS (0.59 ± 0.03 nm vs 0.75 ± 0.03 nm) (Fig. 7). Thus, the intergranular oxidation rate is lower in the as-printed material. Among the microstructure features in the as-printed material, dislocation cell is probably a key factor in the process of intergranular oxidation as it is densely distributed within the grain and near the GBs of SLMed 304L SS.

Fig. 1a$_3$ shows that the SLMed 304L SS has a high density of dislocation cells. The dislocation cells in SLMed SS is composed of high-density dislocations, as evidenced by the neutron diffraction [53]. The dislocation density of SLMed SS is between 10^{14} and 10^{15} m^{-2} [53], while that of wrought annealed state SS is 1.8×10^{11} m^{-2} [54]. The diffusion of atoms is a thermally activated process that can be accelerated (by about three orders of magnitude) by defects such as dislocations. In this work, high dislocation density in SLMed 304L SS probably promotes the diffusion of Cr and enhances the protectiveness of the formed intergranular oxide, thus suppressing the intergranular oxidation and crack initiation [29,55,56]. It should be noted that both SLMed 304L SS and SLMed 304L-1200 SS show apparent GB migration zone beyond the oxide tip (Figs. 5 and 6), indicating that diffusion of Cr is apparent. The GB migration seems more pronounced in SLMed 304L SS than in SLMed 304L-1200 SS (Fig. 5), suggesting that the as-printed microstructure could facilitate the diffusion of Cr. The work by He et al. [57] also suggests that faster diffusion of Cr along GB corresponds to higher resistance to crack initiation. In addition, the plan-view of SSRT samples in Fig. 3 reveals that SLMed 304L SS contains denser outer oxide particles than the other three SSs. Interestingly, the cracks on SLMed 304L SS are always filled with oxide particles. The STEM-EDS results (Fig. 8d, e, f and g) show that the outer oxide particles are Fe-enriched spinel. The outer oxide particles are formed through the precipitation of local cation, indicating that a large number of Fe ions are dissolved into high temperature water from SLMed 304L SS. The fast release of cation from SLMed 304L SS should be related to the high density of dislocations in the matrix. The dense outer oxide particles within the cracks (as shown in Fig. 8) could barricade the ingress of solution, thus further mitigating the intergranular attack. Therefore, the good intergranular oxidation resistance of SLMed 304L SS could be understood from the enhancing effect of dislocation cells on element diffusion and the barricading effect of oxide particles on the ingress of corrosive media in the crack.

4.2.2. Effect of microstructure on the dislocation slip behavior

The strain field measured by DIC (Figs. S4a, b and 10) reveals that there is lower degree of planar slip on the surface of SLMed 304L SS compared to the wrought SS. Planar slip is a typical form of localized deformation, which is related to the high susceptibility to intergranular SCC. Was's group [58,59] investigated the impact of localized deformation on irradiation-assisted SCC of SSs in BWR water and found that the degree of localized deformation is well correlated with the susceptibility to irradiation-assisted SCC. Later on, they [60–62] studied the micromechanics of dislocation channeling in intergranular SCC nucleation and found that the discontinuous intersection between dislocation channel and a single GB could induce very high local stress that stimulates crack nucleation. Although the deformation in planar slip is not as localized as in dislocation channel, it would play a similar role in the SCC initiation of non-irradiated SS. Therefore, SLMed 304L SS has much lower susceptibility to SCC initiation than the wrought SSs partly because it generates no obvious slip step while the wrought SSs show typical planar slip bands during straining.

The difference in dislocation slip behavior should be closely related to the different microstructure features. Among the non-equilibrium microstructure features in SLMed 304L SS, the dense dislocation cells and nano oxide inclusions (shown in Fig. 1b and c) would generate significant effects on dislocation slip behavior. It has been reported that the dislocation cell can serve as stable and "soft" barrier for dislocation motion [63–65]. As such, the dislocation cell is able to hinder but not completely block the gliding of dislocations during plastic straining. Thus, the as-printed material normally exhibits a good combination of strength and ductility. More importantly, the newly nucleated dislocations would be pinned down at the stable dislocation cell boundaries [66–68] and the planar dislocation slip across the grain can be suppressed under small applied plastic strain (Fig. 10). In addition, nano-oxide inclusions are formed during SLM processing (Fig. 1), as have been reported before [69]. Extensive studies [70–72] indicate that the nano-inclusions are amorphous oxide, which can also pin dislocations during deformation. Therefore, under the combined effects of dislocation cells and nano-oxide inclusions, the dislocation motion is

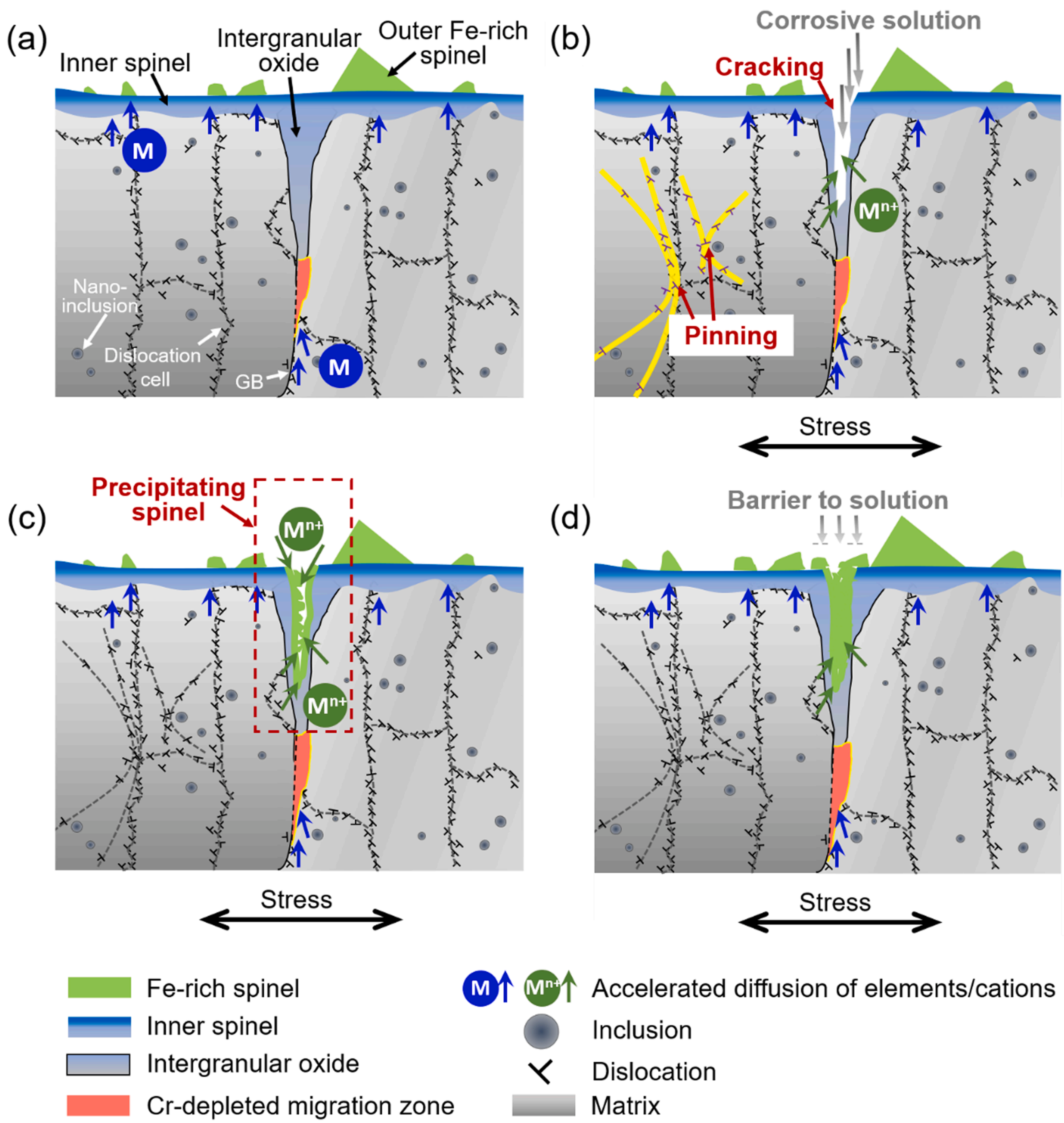

Fig. 12. Schematics of the time evolution of the oxidation and cracking of SLMed 304L SS during the SSRT test. (a) surface oxidation and intergranular oxidation, accompanied by the accelerated diffusion of cations and GB migration in the matrix; (b) dislocations motion, obstruction and intergranular oxide cracking process as stress increasing; (c) crack accelerates oxidation and diffusion of GB, and then the crack is filled with Fe-rich oxides; (d) complete pile up of Fe-rich oxides in the original crack, and the corrosion of GB is inhibited.

effectively hindered in the grain matrix and planar slip is suppressed. In this case, the stress accumulation at the GBs due to slip band/GB interaction can be minimized, thus decreasing the susceptibility to SCC initiation of SLMed 304L SS.

4.3. Insights into SCC mechanism of SLMed 304L SS

This work shows that the SLMed 304L SS has much higher resistance to SCC initiation than the wrought 304 SS. This benefit would undoubtfully make additive manufacturing more desirable for application in nuclear power industry. The mechanism of higher SCC resistance in SLMed 304L SS is schematically shown in Fig. 12. There are dense dislocation cells and randomly distributed nano-inclusions in the SLMed 304L SS matrix. Intergranular preferential oxidation also occurs in SLMed 304L SS as in wrought SS. As the contents of Si and Mn in SLMed 304L SS are greatly reduced, the formed intergranular oxide is less defective and the oxidation rate is low. Thus, the optimized composition of SLMed 304L SS greatly reduces the cracking tendency. In addition, dense dislocations accelerate the diffusion of Cr along the GB to the oxidation front, further enhancing the protectiveness of formed intergranular oxide. Meanwhile, a Cr-depleted GB migration zone forms beyond the intergranular oxide (Fig. 12a). During the SSRT test, dislocations nucleate at imperfections like nano oxide inclusions and dislocation cells (Fig. 12b). The generated dislocations cannot move freely within the grain as the dislocation cells and nano inclusions are stable barriers that block and pin the dislocations. It can be inferred that a large number of dislocations are confined within the grain matrix and the planar slip across the grain is suppressed. As such, the slip band/GB interaction may be reduced and the accumulated dislocation near GB is minimized, thus decreasing the localized stress concentration which is part of the driving force for crack initiation. When the intergranular oxide cracks, corrosive aqueous solution enters into the crack (Fig. 12b) and further promotes the oxidation process by shortening the diffusion path. The volume and depth of intergranular oxidation increase and the GB migration zone gets larger and moves downwards. In the meantime, due to the enhanced diffusion of dislocation cells, the cations released during the oxidation rapidly accumulate and deposit as Fe-rich spinel oxide (Fig. 12c). Such spinel oxide particles partly fill the crack and barricade the ingress of solution. Thus, the oxidation process of GB gradually slows down and the cracking process is mitigated as well (Fig. 12d). The whole process is repeated under the drive of dynamic straining.

5. Conclusions

In this work, the SCC susceptibility of a SLMed 304L SS was studied in high temperature hydrogenated water and compared with those of conventional wrought 304 SSs. The results show that the SLMed 304L SS exhibits significantly superior resistance to SCC initiation due to the optimized chemical composition and as-printed microstructures. The following conclusions can be achieved:

(1) Through plan-view and cross-section evaluation, the order of SCC susceptibility is: SLMed 304L SS $<$ SLMed 304L-1200 SS $<<$ 304-A SS and 304-B SS. The SLMed 304L SS has extremely small cracks, which is filled with Fe-rich spinel and contains a Cr-depleted GB migration zone beyond the intergranular oxide.
(2) The higher SCC resistance of SLMed 304L SS is closely linked to its lower tendency to intergranular oxidation. The improved resistance to intergranular oxidation of SLMed 304L SS is largely attributed to the reduced contents of Si and Mn which are detrimental to the protective of oxide. In addition, the high dislocation density in SLMed 304L SS can accelerate the diffusion of solute atoms, thus further enhancing the resistance to intergranular oxidation and promoting the precipitation of oxide inside the crack which slows down the ingress of corrosive media.
(3) The change in the dislocation slip behavior might further improve the SCC resistance of SLMed 304L SS. Dislocation cells and oxide inclusions in SLMed 304L SS can suppress planar dislocation slip and relieve local stress concentration near GB during plastic deformation.

Declaration of Competing Interest

The authors declare that they have no known competing financial interests or personal relationships that could have appeared to influence the work reported in this paper.

Acknowledgments

The authors gratefully acknowledge the financial support of National Natural Science Foundation of China (no. 51971172), Development Program of the Ministry of Science and Technology of China (no. 2019YFA0209900) and Young Talent Support Plan of Xi'an Jiaotong University. The authors thank Shaojun Wu and Prof. Genshu Zhou of Xi'an Jiaotong University for their assistance in Ni plating. The authors also thank Mr. Wei Wang, Dr. Chaowei Guo and Dr. Peng Zhang of Xi'an Jiaotong University for their help on SEM and TEM characterization, and Dr. Jiao Li and Dr. Chao Li at Instrument Analysis Center of Xi'an Jiaotong University for their help on (S)TEM and EDS characterization. We would also like to thank the following people for useful discussions: Dr. Litao Chang from Shanghai Institute of Applied Physics (Chinese Academy of Sciences) and Dr. Miao Song from Shanghai Jiao Tong University.

Supplementary materials

Supplementary material associated with this article can be found, in the online version, at doi:10.1016/j.actamat.2022.118561.

References

[1] C.Y. Yap, C.K. Chua, Z.L. Dong, Z.H. Liu, D.Q. Zhang, L.E. Loh, S.L. Sing, Review of selective laser melting: materials and applications, Appl. Phys. Rev. 2 (4) (2015) 21.
[2] J.J. Lewandowski, M. Seifi, Metal additive manufacturing: a review of mechanical properties, Annu. Rev. Mater. Res. 46 (1) (2016) 151–186.
[3] G. Sander, J. Tan, P. Balan, O. Gharbi, D.R. Feenstra, L. Singer, S. Thomas, R. G. Kelly, J.R. Scully, N. Birbilis, Corrosion of additively manufactured alloys: a review, Corrosion 74 (12) (2018) 1318–1350.
[4] T.D. Ngo, A. Kashani, G. Imbalzano, K.T.Q. Nguyen, D. Hui, Additive manufacturing (3D printing): a review of materials, methods, applications and challenges, Composit. Part: B 143 (2018) 172–196.
[5] W.E. Frazier, Metal additive manufacturing: a review, J. Mater. Eng. Perform. 23 (6) (2014) 1917–1928.
[6] X. Lou, D. Gandy, Advanced manufacturing for nuclear energy, JOM 71 (8) (2019) 2834–2836.
[7] Y.M. Wang, T. Voisin, J.T. McKeown, J. Ye, N.P. Calta, Z. Li, Z. Zeng, Y. Zhang, W. Chen, T.T. Roehling, R.T. Ott, M.K. Santala, P.J. Depond, M.J. Matthews, A. V. Hamza, T. Zhu, Additively manufactured hierarchical stainless steels with high strength and ductility, Nat. Mater. 17 (1) (2018) 63–71.
[8] H. Wu, G. Fan, An overview of tailoring strain delocalization for strength-ductility synergy, Prog. Mater Sci. 113 (2020), 100675.
[9] J. Hou, W. Chen, Z. Chen, K. Zhang, A. Huang, Microstructure, tensile properties and mechanical anisotropy of selective laser melted 304 L stainless steel, J. Mater. Sci. Technol. 48 (2020) 63–71.
[10] S.J. Zinkle, G.S. Was, Materials challenges in nuclear energy, Acta Mater 61 (3) (2013) 735–758.
[11] S.J. Zinkle, J.T. Busby, Structural materials for fission & fusion energy, Mater. Today 12 (11) (2009) 12–19.
[12] X. Lou, M. Song, P.W. Emigh, M.A. Othon, P.L. Andresen, On the stress corrosion crack growth behaviour in high temperature water of 316 L stainless steel made by laser powder bed fusion additive manufacturing, Corros. Sci. 128 (2017) 140–153.
[13] X. Lou, M.A. Othon, R.B. Rebak, Corrosion fatigue crack growth of laser additively-manufactured 316 L stainless steel in high temperature water, Corros. Sci. 127 (2017) 120–130.
[14] X. Lou, P.L. Andresen, R.B. Rebak, Oxide inclusions in laser additive manufactured stainless steel and their effects on impact toughness and stress corrosion cracking behavior, J. Nucl. Mater. 499 (2018) 182–190.

[15] M. Song, M. Wang, X. Lou, R.B. Rebak, G.S. Was, Radiation damage and irradiation-assisted stress corrosion cracking of additively manufactured 316 L stainless steels, J. Nucl. Mater. 513 (2019) 33–44.
[16] D. Kong, C. Dong, S. Wei, X. Ni, L. Zhang, R. Li, L. Wang, C. Man, X. Li, About metastable cellular structure in additively manufactured austenitic stainless steels, Addit. Manuf. 38 (2021), 101804.
[17] Y. Zhong, L.-E. Rannar, S. Wikman, A. Koptyug, L. Liu, D. Cui, Z. Shen, Additive manufacturing of ITER first wall panel parts by two approaches: selective laser melting and electron beam melting, Fusion Eng. Des. 116 (2017) 24–33.
[18] M.J.K. Lodhi, K.M. Deen, M.C. Greenlee-Wacker, W. Haider, Additively manufactured 316 L stainless steel with improved corrosion resistance and biological response for biomedical applications, Addit. Manuf. 27 (2019) 8–19.
[19] Y. Hong, C. Zhou, Y. Zheng, L. Zhang, J. Zheng, The cellular boundary with high density of dislocations governed the strengthening mechanism in selective laser melted 316 L stainless steel, Mater. Sci. Eng. A 799 (2021), 140279.
[20] D. Kong, X. Ni, C. Dong, L. Zhang, C. Man, J. Yao, K. Xiao, X. Li, Heat treatment effect on the microstructure and corrosion behavior of 316 L stainless steel fabricated by selective laser melting for proton exchange membrane fuel cells, Electrochim. Acta 276 (2018) 293–303.
[21] T. Moss, W. Kuang, G.S. Was, Stress corrosion crack initiation in Alloy 690 in high temperature water, Curr. Opin. Solid State Mater. Sci. 22 (1) (2018) 16–25.
[22] R.M. Horn, G.M. Gordon, F.P. Ford, R.L. Cowan, Experience and assessment of stress corrosion cracking in L-grade stainless steel BWR internals, Nucl. Eng. Des. 174 (3) (1997) 313–325.
[23] M. McMurtrey, C. Sun, R.E. Rupp, C.H. Shiau, R. Hanbury, N. Jerred, R. O'Brien, Investigation of the irradiation effects in additively manufactured 316 L steel resulting in decreased irradiation assisted stress corrosion cracking susceptibility, J. Nucl. Mater. 545 (2021), 152739.
[24] W. Kuang, G.S. Was, The effects of grain boundary carbide density and strain rate on the stress corrosion cracking behavior of cold rolled Alloy 690, Corros. Sci. 97 (2015) 107–114.
[25] W. Kuang, X. Feng, H. Yue, G.S. Was, X. Hao, Insights into the roles of intergranular carbides in the initiation of intergranular stress corrosion cracking of alloy 690 in simulated PWR primary water, Corros. Sci. 196 (2022), 110048.
[26] F. Di Gioacchino, J.Q. da Fonseca, Plastic strain mapping with sub-micron resolution using digital image correlation, Exp. Mech. 53 (5) (2013) 743–754.
[27] W. Kuang, H. Yue, X. Feng, B. Yang, C. Guo, A novel test technique for the mechanistic study of initiation of environmentally assisted cracking on a Ni–30Cr–10Fe alloy in simulated pressurized water reactor primary water, Scripta Mater. 189 (2020) 122–128.
[28] J. Blaber, B. Adair, A. Antoniou, Ncorr: open-source 2D digital image correlation matlab software, Exp. Mech. 55 (6) (2015) 1105–1122.
[29] L. Chang, M.G. Burke, F. Scenini, Stress corrosion crack initiation in machined type 316 L austenitic stainless steel in simulated pressurized water reactor primary water, Corros. Sci. 138 (2018) 54–65.
[30] P. Deng, Q.J. Peng, E.H. Han, W. Ke, C. Sun, Proton irradiation assisted localized corrosion and stress corrosion cracking in 304 nuclear grade stainless steel in simulated primary PWR water, J. Mater. Sci. Technol. 65 (2021) 61–71.
[31] W. Kuang, G.S. Was, C. Miller, M. Kaufman, T. Alam, B. Gwalani, R. Banerjee, The effect of cold rolling on grain boundary structure and stress corrosion cracking susceptibility of twins in alloy 690 in simulated PWR primary water environment, Corros. Sci. 130 (2018) 126–137.
[32] S. Lozano-Perez, K. Kruska, I. Iyengar, T. Terachi, T. Yamada, The role of cold work and applied stress on surface oxidation of 304 stainless steel, Corros. Sci. 56 (2012) 78–85.
[33] S. Wang, S. Zhang, J. Xie, X. Feng, M. Song, G.S. Was, W. Kuang, Clarifying the mitigation effect of proton irradiation on the intergranular oxidation of 316 L stainless steel in high temperature water, Acta Mater 241 (2022), 118408.
[34] W. Kuang, X. Feng, D. Du, M. Song, M. Wang, G.S. Was, A high-resolution characterization of irradiation-assisted stress corrosion cracking of proton-irradiated 316 L stainless steel in simulated pressurized water reactor primary water, Corros. Sci. 199 (2022), 110187.
[35] K. Kruska, S. Lozano-Perez, D.W. Saxey, T. Terachi, T. Yamada, G.D.W. Smith, 3D atom-probe characterization of stress and cold-work in stress corrosion cracking of 304 stainless steel, in: Proceedings of the 15th International Conference on Environmental Degradation of Materials in Nuclear Power System, 2011.
[36] W. Kuang, E.-H. Han, X. Wu, J. Rao, Microstructural characteristics of the oxide scale formed on 304 stainless steel in oxygenated high temperature water, Corros. Sci. 52 (11) (2010) 3654–3660.
[37] W. Kuang, M. Song, G.S. Was, Insights into the stress corrosion cracking of solution annealed alloy 690 in simulated pressurized water reactor primary water under dynamic straining, Acta Mater 151 (2018) 321–333.
[38] W. Kuang, G.S. Was, A high-resolution characterization of the initiation of stress corrosion crack in Alloy 690 in simulated pressurized water reactor primary water, Corros. Sci. 163 (2020), 108243.
[39] P.M. Scott, P. Combrade, General corrosion and stress corrosion cracking of Alloy 600 in light water reactor primary coolants, J. Nucl. Mater. 524 (2019) 340–375.
[40] D. Du, K. Sun, G.S. Was, IASCC of neutron irradiated 316 stainless steel to 125 dpa, Mater. Charact. 173 (2021), 110897.
[41] M. Meisnar, A. Vilalta-Clemente, M. Moody, K. Arioka, S. Lozano-Perez, A mechanistic study of the temperature dependence of the stress corrosion crack growth rate in SUS316 stainless steels exposed to PWR primary water, Acta Mater. 114 (2016) 15–24.
[42] Q. Peng, J. Hou, Y. Takeda, T. Shoji, Effect of chemical composition on grain boundary microchemistry and stress corrosion cracking in Alloy 182, Corros. Sci. 67 (2013) 91–99.
[43] P.L. Andresen, M.M. Morra, Effects of Si on SCC of irradiated and unirradiated stainless steels and nickel alloys, in: Proceedings of the 12th International Conference on Environmental Degradation of Materials in Nuclear Power System, 2005.
[44] P.L. Andresen, M.M. Morra, Stress corrosion cracking of stainless steels and nickel alloys in high-temperature water, Corrosion 64 (1) (2008) 15–29.
[45] G.F. Li, Y. Kaneshima, T. Shoji, Effects of impurities on environmentally assisted crack growth of solution-annealed austenitic steels in primary water at 325 °C, Corrosion 56 (5) (2000) 460–469.
[46] W. Kuang, J. Hesterberg, G.S. Was, The effect of post-irradiation annealing on the stress corrosion crack growth rate of neutron-irradiated 304 L stainless steel in boiling water reactor environment, Corros. Sci. 161 (2019), 108183.
[47] L. Legras, B. Marylou, F. Elodie, C. Priscille, M. Remi, M. Salem, T. Jinane, R. Menand, TEM investigations of the microstructure and oxides at the tip of intergranular cracks of a baffle former bolt irradiated up to 10 dpa, in: FONTEVRAUD 9, Avignon, France, 2018.
[48] J. Dong, X. Feng, X. Hao, W. Kuang, The environmental degradation behavior of FeNiMnCr high entropy alloy in high temperature hydrogenated water, Scripta Mater. 204 (2021), 114127.
[49] K. Lutton Cwalina, C.R. Demarest, A.Y. Gerard, J.R. Scully, Revisiting the effects of molybdenum and tungsten alloying on corrosion behavior of nickel-chromium alloys in aqueous corrosion, Curr. Opin. Solid State Mater. Sci. 23 (3) (2019) 129–141.
[50] J.D. Henderson, A. Seyeux, S. Zanna, M.C. Biesinger, D.W. Shoesmith, J.J. Noël, P. Marcus, Investigating the transport mechanisms governing the oxidation of Hastelloy BC-1 by in situ ToF-SIMS, Corros. Sci. 159 (2019), 108138.
[51] X.X. Yu, A. Gulec, C.M. Andolina, E.J. Zeitchick, K. Gusieva, J.C. Yang, J.R. Scully, J.H. Perepezko, L.D. Marks, In situ observations of early stage oxidation of Ni-Cr and Ni-Cr-Mo alloys, Corrosion 74 (9) (2018) 939–946.
[52] L. Wang, A. Seyeux, P. Marcus, Ion transport mechanisms in the oxide film formed on 316 L stainless steel surfaces studied by ToF-SIMS with(18)O(2)Isotopic tracer, J. Electrochem. Soc. 167 (10) (2020), 101511.
[53] R. Pokharel, L. Balogh, D.W. Brown, B. Clausen, G.T. Gray, V. Livescu, S.C. Vogel, S. Takajo, Signatures of the unique microstructure of additively manufactured steel observed via diffraction, Scripta Mater. 155 (2018) 16–20.
[54] S. Murugesan, P. Kuppusami, E. Mohandas, M. Vijayalakshmi, X-ray diffraction Rietveld analysis of cold worked austenitic stainless steel, Mater. Lett. 67 (1) (2012) 173–176.
[55] C. Ma, Q. Peng, J. Mei, E.-.H. Han, W. Ke, Microstructure and corrosion behavior of the heat affected zone of a stainless steel 308L-316 L weld joint, J. Mater. Sci. Technol. 34 (10) (2018) 1823–1834.
[56] L. Chang, M.G. Burke, F. Scenini, Understanding the effect of surface finish on stress corrosion crack initiation in warm-forged stainless steel 304 L in high-temperature water, Scripta Mater 164 (2019) 1–5.
[57] M.-.R. He, D.C. Johnson, G.S. Was, I.M. Robertson, The role of grain boundary microchemistry in irradiation-assisted stress corrosion cracking of a Fe-13Cr-15Ni alloy, Acta Mater. 138 (2017) 61–71.
[58] Z. Jiao, G.S. Was, Impact of localized deformation on IASCC in austenitic stainless steels, J. Nucl. Mater. 408 (3) (2011) 246–256.
[59] G.S. Was, D. Farkas, I.M. Robertson, Micromechanics of dislocation channeling in intergranular stress corrosion crack nucleation, Curr. Opin. Solid State Mater. Sci. 16 (3) (2012) 134–142.
[60] M.D. McMurtrey, G.S. Was, B. Cui, I. Robertson, L. Smith, D. Farkas, Strain localization at dislocation channel–grain boundary intersections in irradiated stainless steel, Int. J. Plast. 56 (2014) 219–231.
[61] M.D. McMurtrey, B. Cui, I. Robertson, D. Farkas, G.S. Was, Mechanism of dislocation channel-induced irradiation assisted stress corrosion crack initiation in austenitic stainless steel, Curr. Opin. Solid State Mater. Sci. 19 (5) (2015) 305–314.
[62] D.C. Johnson, B. Kuhr, D. Farkas, G.S. Was, Quantitative linkage between the stress at dislocation channel – Grain boundary interaction sites and irradiation assisted stress corrosion crack initiation, Acta Mater. 170 (2019) 166–175.
[63] L. Liu, Q. Ding, Y. Zhong, J. Zou, J. Wu, Y.-.L. Chiu, J. Li, Z. Zhang, Q. Yu, Z. Shen, Dislocation network in additive manufactured steel breaks strength–ductility trade-off, Mater. Today 21 (4) (2018) 354–361.
[64] Z. Li, B. He, Q. Guo, Strengthening and hardening mechanisms of additively manufactured stainless steels: the role of cell sizes, Scripta Mater. 177 (2020) 17–21.
[65] X. Wang, B. Zheng, K. Yu, S. Jiang, E.J. Lavernia, J.M. Schoenung, The role of cell boundary orientation on mechanical behavior: a site-specific micro-pillar characterization study, Addit. Manuf. 46 (2021), 102154.
[66] D. Riabov, A. Leicht, J. Ahlström, E. Hryha, Investigation of the strengthening mechanism in 316 L stainless steel produced with laser powder bed fusion, Mater. Sci. Eng. A 822 (2021), 141699.
[67] J.G. Kim, J.B. Seol, J.M. Park, H. Sung, S.H. Park, H.S. Kim, Effects of cell network structure on the strength of additively manufactured stainless steels, Met. Mater. Int. 27 (8) (2021) 2614–2622.
[68] Z. Li, Y. Cui, W. Yan, D. Zhang, Y. Fang, Y. Chen, Q. Yu, G. Wang, H. Ouyang, C. Fan, Q. Guo, D.-.B. Xiong, S. Jin, G. Sha, N. Ghoniem, Z. Zhang, Y.M. Wang, Enhanced strengthening and hardening via self-stabilized dislocation network in additively manufactured metals, Mater. Today 50 (2021) 79–88.
[69] P. Deng, M. Karadge, R.B. Rebak, V.K. Gupta, B.C. Prorok, X. Lou, The origin and formation of oxygen inclusions in austenitic stainless steels manufactured by laser powder bed fusion, Addit. Manuf. 35 (2020), 101334.

[70] Y. Zhong, L. Liu, J. Zou, X. Li, D. Cui, Z. Shen, Oxide dispersion strengthened stainless steel 316 L with superior strength and ductility by selective laser melting, J. Mater. Sci. Technol. 42 (2020) 97–105.
[71] K. Saeidi, L. Kvetková, F. Lofaj, Z. Shen, Austenitic stainless steel strengthened by the in situ formation of oxide nanoinclusions, RSC Adv 5 (27) (2015) 20747–20750.
[72] D. Kong, C. Dong, X. Ni, Z. Liang, X. Li, In-situ observation of asymmetrical deformation around inclusion in a heterogeneous additively manufactured 316 L stainless steel, J. Mater. Sci. Technol. 89 (2021) 133–140.